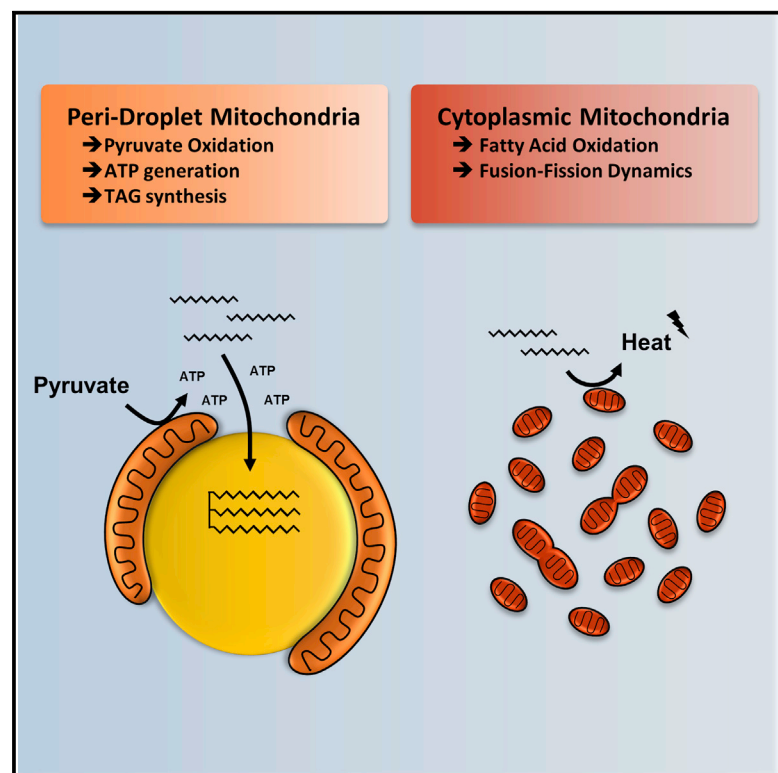


Cell Metabolism

Mitochondria Bound to Lipid Droplets Have Unique Bioenergetics, Composition, and Dynamics that Support Lipid Droplet Expansion

Graphical Abstract



Authors

Ilan Y. Benador, Michaela Veliova, Kiana Mahdavian, ..., Barbara E. Corkey, Marc Liesa, Orian S. Shirihai

Correspondence

mliesa@mednet.ucla.edu (M.L.), oshirihai@mednet.ucla.edu (O.S.S.)

In Brief

Benador et al. report on a distinct mitochondrial population associated with lipid droplets in the interscapular brown adipose tissue. Peridroplet mitochondria have enhanced bioenergetic capacity, reduced β -oxidation capacity, support lipid droplet expansion by providing ATP for triacylglyceride synthesis, and maintain a distinct protein composition due to low fusion-fission dynamics.

Highlights

- Peridroplet mitochondria (PDM) have enhanced bioenergetic capacity
- Peridroplet mitochondria have low fatty acid oxidation capacity
- PDM support lipid droplet expansion by providing ATP for triacylglyceride synthesis
- Distinct fusion-fission dynamics separate PDM from cytoplasmic mitochondria



Mitochondria Bound to Lipid Droplets Have Unique Bioenergetics, Composition, and Dynamics that Support Lipid Droplet Expansion

Ilan Y. Benador,^{1,2} Michaela Veliova,^{1,10} Kiana Mahdaviani,^{2,10} Anton Petcherski,¹ Jakob D. Wikstrom,^{3,4} Essam A. Assali,^{1,5} Rebeca Acín-Pérez,¹ Michaël Shum,¹ Marcus F. Oliveira,⁶ Saverio Cinti,⁷ Carole Sztalryd,⁸ William D. Barshop,⁹ James A. Wohlschlegel,⁹ Barbara E. Corkey,² Marc Liesa,^{1,*} and Orian S. Shirihai^{1,2,5,11,*}

¹Division of Endocrinology, Department of Medicine, and Department of Molecular and Medical Pharmacology, David Geffen School of Medicine at UCLA, Los Angeles, CA, USA

²Obesity Research Center, Department of Medicine, Boston University School of Medicine, Boston, MA, USA

³Dermatology and Venereology Unit, Department of Medicine, Karolinska Institutet, Stockholm, Sweden

⁴Department of Dermato-Venereology, Karolinska University Hospital, Stockholm, Sweden

⁵Department of Clinical Biochemistry, School of Medicine, Ben Gurion University of The Negev, Beer-Sheva, Israel

⁶Institute of Medical Biochemistry Leopoldo de Meis, Universidade Federal do Rio de Janeiro, Rio de Janeiro, Brazil

⁷Department of Experimental and Clinical Medicine, University of Ancona, Ancona, Italy

⁸Department of Medicine, School of Medicine, University of Maryland Baltimore, MD, USA

⁹Department of Biological Chemistry, David Geffen School of Medicine at UCLA, Los Angeles, CA, USA

¹⁰These authors contributed equally

¹¹Lead Contact

*Correspondence: mliesa@mednet.ucla.edu (M.L.), oshirihai@mednet.ucla.edu (O.S.S.)

<https://doi.org/10.1016/j.cmet.2018.03.003>

SUMMARY

Mitochondria associate with lipid droplets (LDs) in fat-oxidizing tissues, but the functional role of these peridroplet mitochondria (PDM) is unknown. Microscopic observation of interscapular brown adipose tissue reveals that PDM have unique protein composition and cristae structure and remain adherent to the LD in the tissue homogenate. We developed an approach to isolate PDM based on their adherence to LDs. Comparison of purified PDM to cytoplasmic mitochondria reveals that (1) PDM have increased pyruvate oxidation, electron transport, and ATP synthesis capacities; (2) PDM have reduced β -oxidation capacity and depart from LDs upon activation of brown adipose tissue thermogenesis and β -oxidation; (3) PDM support LD expansion as Perilipin5-induced recruitment of mitochondria to LDs increases ATP synthase-dependent triacylglyceride synthesis; and (4) PDM maintain a distinct protein composition due to uniquely low fusion-fission dynamics. We conclude that PDM represent a segregated mitochondrial population with unique structure and function that supports triacylglyceride synthesis.

INTRODUCTION

Studies have shown that mitochondria contact lipid droplets (LDs) in tissues with fatty acid storage and oxidation capacity, including brown adipose tissue (BAT) (Boutant et al., 2017), heart (Wang et al., 2013), and type I skeletal muscle (Tarnopolsky et al., 2007). Furthermore, mitochondria-LD association was shown to

be highly regulated by Perilipin5 (Plin5), a LD-coating protein highly expressed in fat-oxidizing tissues (Wang et al., 2011). The high degree of regulation and tissue specificity supports the concept that peridroplet mitochondria (PDM) play a specialized role in fat metabolism. However, it remains unclear whether PDM promote lipid oxidation (Rambold et al., 2015), lipid storage (Nguyen et al., 2017; Stone et al., 2009; Wang et al., 2011), or both.

In this study, we sought to determine the role of PDM in a system in which a robust shift can occur between fat storage and oxidation. BAT acutely turns on uncoupled lipid oxidation upon adrenergic stimulation (Cannon and Nedergaard, 2004). Functional specialization and segregation of mitochondrial subpopulations may allow BAT mitochondria to perform the contradictory tasks of uncoupled fatty acid oxidation and ATP generation for fatty acid activation by coenzyme A (CoA) addition. However, it remains unclear whether functional specialization and segregation are possible in brown adipocytes, where fusion and fission continuously equilibrate the content across the mitochondrial population within each adipocyte (Wikstrom et al., 2014). Furthermore, there are currently no established methods to isolate PDM, leaving their function, composition, and bioenergetics unknown.

In this study, we developed an approach to isolate PDM from BAT based on their adherence to LDs. Our results demonstrate that PDM represent a segregated mitochondrial subpopulation with distinct composition, bioenergetics, and dynamics that support triacylglyceride (TAG) synthesis.

RESULTS

Isolation of Peridroplet Mitochondria by Differential Centrifugation

Little is currently known about PDM due to the lack of reliable methods to selectively isolate PDM. The tight association



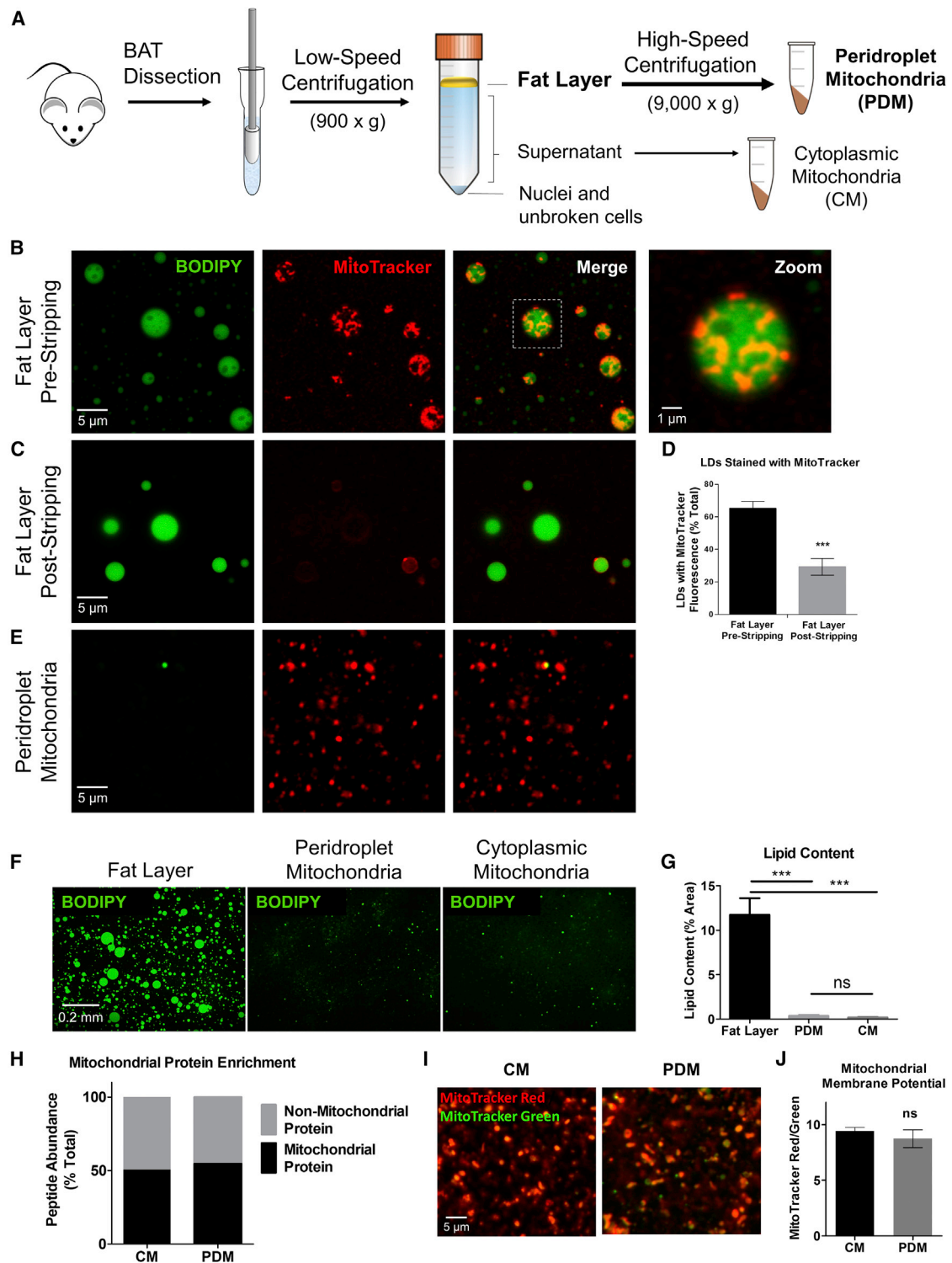


Figure 1. Isolation of Peridroplet Mitochondria by Differential Centrifugation

(A) Schematic representation of peridroplet (PDM) and cytoplasmic (CM) mitochondrial isolation from interscapular brown adipose tissue (BAT). BAT was dissected from mice and homogenized with glass-Teflon dounce homogenizer. Low-speed centrifugation separated the fat layer containing PDM from supernatant containing CM. High-speed centrifugation stripped PDM from lipid droplets (LDs) and pelleted CM from the supernatant. Note that some mitochondrial isolation protocols discard the fat layer and/or begin with high-speed centrifugation step.

(B–E) PDM are stripped from LDs by high-speed centrifugation.

(legend continued on next page)

between mitochondria and LDs observed in electron micrographs (EMs) (Wikstrom et al., 2014) and in biochemical studies (Yu et al., 2015) led us to hypothesize that mitochondria-LD association could withstand mechanical cell disruption. To test this, we disrupted interscapular BAT using a dounce homogenizer, separated the fat layer by low-speed centrifugation, and co-stained it with the neutral lipid dye BODIPY 493/503 (BODIPY) and the mitochondrial dye MitoTracker deep red (MitoTracker) (Figure 1A). Super-resolution confocal microscopy revealed numerous LDs surrounded by tubular MitoTracker-stained structures, suggesting that mitochondria-LD association was preserved in the fat layer (Figure 1B). Next, to separate PDM from LDs, we centrifuged the fat layer at high speed, a procedure previously shown to strip LD proteins (Ding et al., 2013). The stripped fat layer contained more than 50% fewer LDs with MitoTracker fluorescence (Figures 1C and 1D), suggesting that LDs were effectively stripped of PDM. The resulting PDM pellet contained MitoTracker-positive particles and little to no BODIPY staining (Figure 1E), suggesting that PDM were successfully separated from LDs. To confirm that PDM were not contaminated with LD remnants, we quantified the LD content under low-magnification microscopy (Figures 1F and 1G). Low-magnification images revealed that PDM pellet had more than 95% lower LD content compared to the fat layer (Figure 1G). Furthermore, the level of LD contamination within the PDM pellet was similar to the LD contamination within the cytoplasmic mitochondria (CM) pellet isolated from the supernatant (Figures 1A and 1G). These results suggest that LDs were effectively removed from PDM by differential centrifugation.

Since differential centrifugation results in relatively crude preparations, we next determined the mitochondrial protein content in CM and PDM fractions by mass spectrometry. Protein annotation using MitoCarta2.0 (Calvo et al., 2016) revealed that 5,969 out of 10,935 (54.5%) identified peptides belonged to mitochondrial proteins in PDM compared to 5,979 out of 11,812 (50.6%) in CM (Figure 1H). Furthermore, analysis of previously published BAT mitochondria proteomics data revealed a 46.9% enrichment of mitochondrial protein (Forner et al., 2009). These results suggest that mitochondrial protein enrichment in CM and PDM fractions were comparable and within the range of previously published methods.

Next, to determine whether CM and PDM preparations can generate a similar membrane potential, we stained the preparations with the membrane potential-sensitive rosamine dye MitoTracker Red. To control for mitochondrial mass, we co-stained preparations with the mitochondrial protein dye MitoTracker Green (Cottet-Rousselle et al., 2011). Fluorescence microscopy revealed no significant differences in the MitoTracker Red-to-Green fluorescence ratio between CM and

PDM (Figures 1I and 1J), suggesting that CM and PDM preparations were equally capable of generating a membrane potential.

Peridroplet Mitochondria Have Increased Respiratory Capacity

To determine the respiratory capacity of PDM, we measured their oxygen consumption rate using Seahorse XF96 extracellular flux analyzer. Isolated PDM and CM were loaded into different wells of the same Seahorse plate and assayed with pyruvate and malate as fuels. Prior to the assay, we confirmed that equal levels of mitochondrial protein and functional mitochondria were present in CM and PDM preparations by mass spectrometry analysis (Figure 1H) and membrane potential imaging (Figures 1I and 1J), respectively. Furthermore, we confirmed that equal mitochondrial mass was loaded into the XF96 flux analyzer plate by directly staining and imaging the wells with MitoTracker (Figures 2A and 2B).

PDM assayed using pyruvate and malate as fuels showed a 2-fold increase in both ATP-synthesizing respiration (state III) and maximal respiratory capacity induced by uncoupling with FCCP (maximal) when compared to CM (Figures 2C–2E). Enhanced ATP synthesis and maximal electron transport capacities in PDM were not limited to pyruvate oxidation since a similar increase was observed when assayed with the fuel succinate (Figure S1).

To determine whether increased PDM respiratory capacity is associated with higher capacity of respiratory enzyme complexes, we next assessed the activity of individual complexes in isolated mitochondria. Cytochrome *c* oxidase (COX) activity was determined by measuring the oxygen consumption rate driven by TMPD/ascorbate. We injected antimycin and rotenone at the start of the assay and the COX-specific inhibitor sodium azide at the end of the assay to confirm that TMPD/ascorbate-driven respiration was specific to COX activity. TMPD/ascorbate-driven respiration was 68% ± 27.5% higher in PDM compared to CM (Figures 2F and 2G), confirming that isolated PDM have higher COX activity compared to CM.

Next, we determined ATP synthase function in isolated mitochondria using firefly luciferase luminescence. We determined the optimal concentration of reagents and photometric measurement settings using HPLC-purified ATP standards and controlled for non-OXPHOS ATP synthesis using the ATP synthase inhibitor oligomycin. PDM had a 210.4% ± 62.8% higher rate of luminescence increase compared to CM (Figures 2H and 2I), confirming that isolated PDM have higher ATP synthesis capacity compared to CM.

Next, to determine whether higher respiratory capacity observed in isolated PDM can be detected in living cells, we

(B and C) Super-resolution confocal images of the fat layer before (B) and after (C) high-speed centrifugation. LDs were marked by the neutral BODIPY 493/503 fluorescent dye (BODIPY) and mitochondria by MitoTracker deep red dye (MitoTracker). Note the tubular structures staining positively for MitoTracker on LDs. (D) Quantification of LDs with MitoTracker staining in the fat layer pre- and post-stripping by high-speed centrifugation. 11,744 LDs were assessed in total.

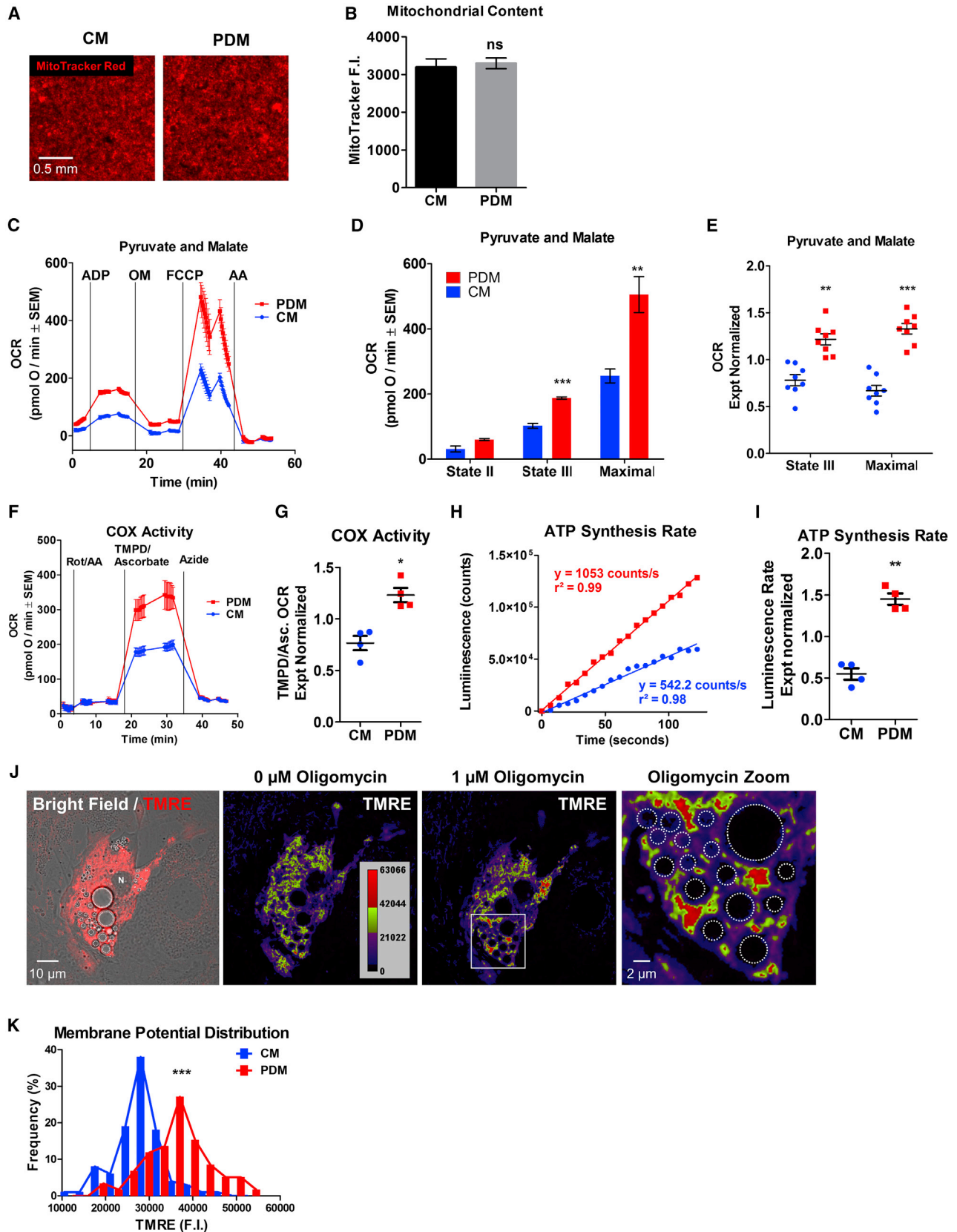
(E) Super-resolution confocal image of PDM pellet separated from fat layer by high-speed centrifugation.

(F and G) Low-magnification (20×) images of the fat layer, PDM pellet, and CM pellet (F) and LD quantification (G). LD content was assessed by BODIPY staining. 5–6 technical replicates per group. $n = 3$ independent isolations. One-way ANOVA with Tukey post-test.

(H) Mass spectrometry analysis of relative mitochondrial protein content of CM and PDM preparations.

(I and J) Analysis of CM and PDM membrane potential by fluorescence microscopy (I) and quantification (J) of CM and PDM double stained with the membrane potential-sensitive dye MitoTracker Red and the mitochondrial protein dye MitoTracker Green. $n = 15$ –22 images per group from 3 independent isolations.

Data are expressed as means ± SEM. ns $p > 0.05$, *** $p < 0.0001$.



(legend on next page)

assessed mitochondrial membrane potential using the reversible membrane potential-sensitive dye tetramethylrhodamine-ethyl-ester-perchlorate (TMRE) in primary brown adipocytes. TMRE fluorescence intensity was not significantly different between CM and PDM at baseline, suggesting that increased PDM proton pumping by electron transport complexes may be matched by higher proton flux through ATP synthase. If this were the case, we reasoned that blocking ATP synthase will cause an acute hyperpolarization of PDM as compared to CM. Indeed, oligomycin treatment revealed PDM with higher TMRE fluorescence intensity compared to CM (Figures 2J and 2K), suggesting that PDM have a higher proton efflux rate compared to CM. Taken together, these results suggest that PDM have enhanced oxidative phosphorylation capacity.

Peridroplet Mitochondria Have Increased Levels of Cytochrome c Oxidase, ATP Synthase, and Super Complex I+III Assembly

We reasoned that increased electron transport and ATP synthesis capacities in PDM could result from increased expression levels of OXPHOS complexes. To test this, we assessed the protein levels of each OXPHOS complex by western blot analysis of complex subunits. We confirmed that equal amounts of protein were loaded by staining western blot membranes with the non-specific protein dye Ponceau S (Figure 3A). To control for mitochondrial protein loading, we normalized bands to the mitochondrial marker TOM20, which did not vary significantly between samples (Figures S2A and S2B).

Western blot analysis revealed that PDM have $15.6\% \pm 4.5\%$ higher levels of cytochrome *c* oxidase subunit 4 (COX4) protein and $8.7\% \pm 4.8\%$ higher ATP synthase subunit α (ATP5a1) protein relative to CM (Figures 3B and 3C). We confirmed that detected differences were independent of loading and band

saturation by performing a dilution blot and histogram analysis, respectively (Figures S2C–S2F). We observed no significant differences in the protein levels of complex I, complex II, or complex III subunits (Figures 3B and 3C). Given the relatively small differences in complex protein levels, we rationalized that enhanced PDM respiratory capacity could be due to increased assembly of respiratory super complexes (Lapuente-Brun et al., 2013; Rosca et al., 2008). To test this, we measured super complex assembly by blue native PAGE. Remarkably, blue native PAGE revealed $29.5\% \pm 8.2\%$ higher levels of complex I + complex III super assembly in PDM relative to CM (Figures 3D and 3E). These results suggest that specialized OXPHOS protein composition and super assembly may contribute to enhanced PDM respiratory capacity.

High Levels of Cytochrome c Oxidase and ATP Synthase Are Preferentially Localized to PDM

To determine the relative levels of OXPHOS proteins in CM and PDM within intact brown adipocytes, we next measured protein levels by immunofluorescence. We confirmed antibody specificity by probing a whole western blot membrane with each individual antibody and exclusively detecting a single band corresponding to the protein of interest (Figure S2G). Super-resolution confocal imaging of immunostained cells revealed heterogeneous distribution of OXPHOS protein in PDM and CM populations (Figures 3F–3I). Subcellular distribution analysis revealed that mitochondria with the highest levels of COX4 and ATP synthase α are exclusively PDM. Remarkably, some LDs were surrounded by ATP synthase-rich PDM, while other LDs within the same cell were surrounded by PDMs with lower ATP synthase levels comparable to CM. This remarkable heterogeneity may explain the relatively small changes that we detected by

Figure 2. Peridroplet Mitochondria Have Enhanced Bioenergetic Capacity

(A–I) Peridroplet (PDM) and cytoplasmic (CM) mitochondria isolated from brown adipose tissue (BAT).

(A) Fluorescence microscopy images of Seahorse respirometry plate wells containing isolated CM and PDM stained with MitoTracker Red.

(B) Quantification of MitoTracker Red fluorescence intensity (F.I.) in Seahorse wells loaded with CM or PDM. 5–7 wells quantified per condition.

(C) Representative traces of oxygen consumption rates (OCRs) of isolated PDM and CM driven with pyruvate+malate. ADP, oligomycin, FCCP, and antimycin were sequentially injected to assess mitochondrial respiratory states. 4–6 technical replicates per group.

(D) Quantification of OCR at different mitochondrial respiratory states in representative experiment. State II quantifies respiration driven by proton leak (no ATP synthesis), state III quantifies respiration driven by ATP synthesis, and maximal respiration quantifies maximal electron transport activity induced by the chemical uncoupler FCCP. 6 technical replicates per group.

(E) Quantification of mitochondrial respiratory states in $n = 8$ independent experiments. For each individual experiment, average OCR values of CM and PDM were normalized to the average OCR of all mitochondria (see [Quantification and Statistical Analysis](#) for complete equations).

(F and G) Cytochrome *c* oxidase activity in PDM and CM isolated from BAT.

(F) Representative traces of oxygen consumption rate (OCR) of isolated PDM and CM driven with the cytochrome *c* oxidase-specific substrates TMPD+Ascorbate. Rotenone and antimycin were injected in the beginning of the assay to extinguish cytochrome *c* reduction by complex I and complex III. The COX-specific inhibitor sodium azide was injected at the end of the assay to control for non-COX oxygen consumption. 5 technical replicates per group.

(G) Quantification of COX activity in $n = 4$ independent isolations. Data were normalized as in (E).

(H and I) ATP synthase activity in PDM and CM isolated from BAT.

(H) Representative traces of luciferase luminescence assay in isolated mitochondria normalized to baseline. ATP synthesis rates were determined by the rate of luminescence gain.

(I) Quantification of ATP synthase activity in $n = 4$ independent isolations. Data were normalized as in (E).

(J and K) Confocal imaging of living cultured brown adipocytes stained with membrane potential-sensitive dye TMRE.

(J) Confocal imaging before and after addition of the ATP synthase inhibitor oligomycin. Bright-field image was used to identify LDs. TMRE images were pseudo-colored for quantitative display (see calibration bar). Note that PDM had higher fluorescence than CM after oligomycin treatment. White dashed circles denote LDs, white N denotes the nucleus, and white square denotes zoomed region.

(K) Quantification of TMRE fluorescence intensity in oligomycin-treated brown adipocytes. 159 mitochondria were assessed in total. $n = 33$ cells collected in 6 independent experiments.

Data are expressed as means \pm SEM. ns $p > 0.05$, * $p < 0.05$, ** $p < 0.001$, *** $p < 0.0001$.

See also [Figure S1](#).

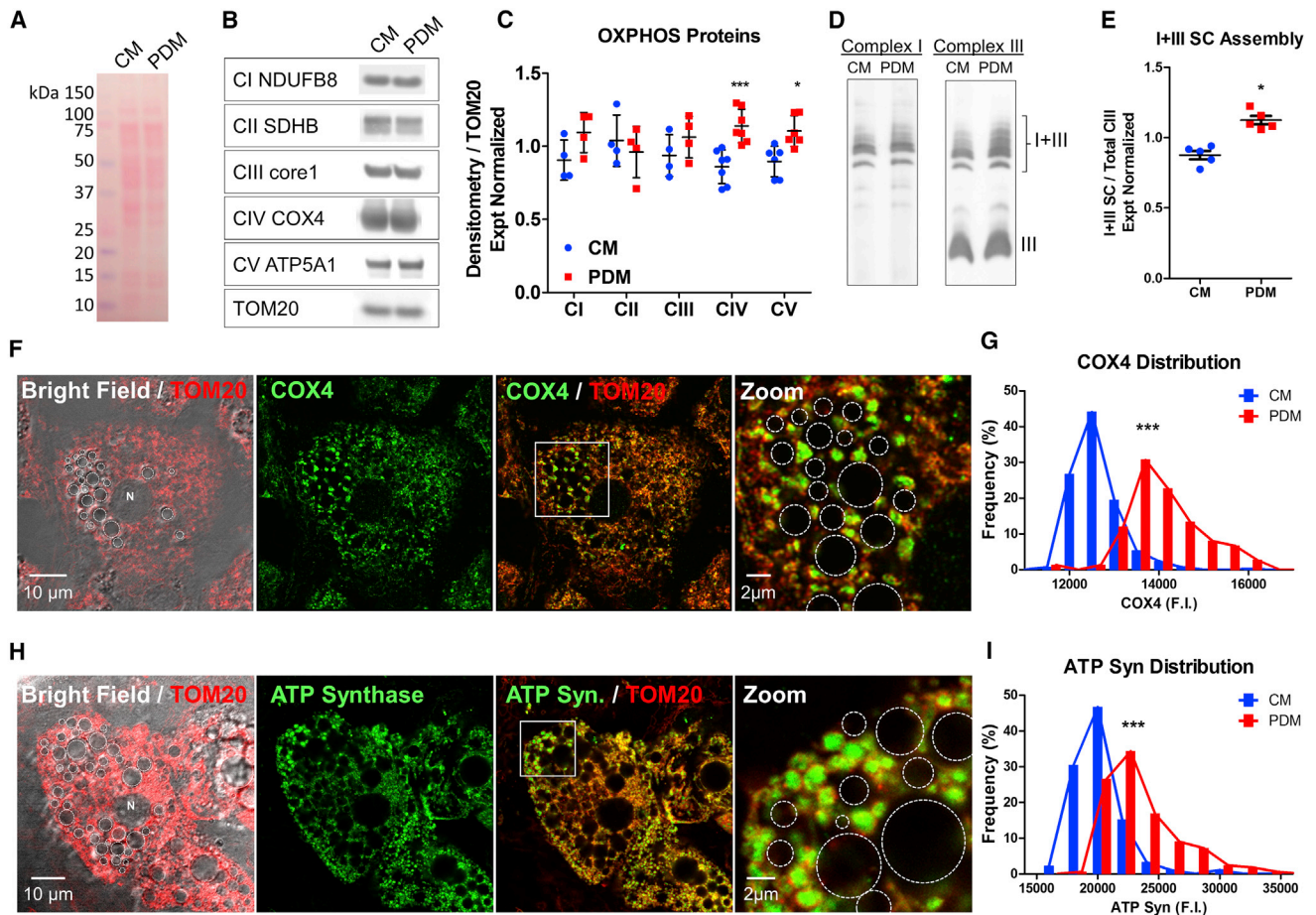


Figure 3. Peridroplet Mitochondria Have Increased Levels of Cytochrome c Oxidase, ATP Synthase, and Super Complex I+III Assembly

(A–C) Western blot analysis of peridroplet (PDM) and cytoplasmic (CM) mitochondria isolated from brown adipose tissue (BAT).

(A) Western blot of isolated CM and PDM stained with the dye Ponceau S for total protein loading.

(B) Western blot probed with antibodies of OXPHOS complex subunits I–V (CI–CV) and TOM20 as a loading control.

(C) Quantification of OXPHOS complex subunits normalized to TOM20 loading control in $n = 4–7$ independent isolations. For each individual experiment, average values detected in CM and PDM were normalized to the average subunit protein levels of all mitochondria (see [Quantification and Statistical Analysis](#) for complete equations).

(D and E) Western blot of blue native PAGE of PDM and CM isolated from BAT.

(D) Western blot of assembled complex I and complex III in isolated mitochondria.

(E) Quantification of complex III assembled into I+III super complexes relative to total complex III. $n = 5$ independent isolations. Data were normalized as in (C).

(F–I) Super-resolution confocal imaging of fixed cultured brown adipocytes (no adrenergic stimulation).

(F) Brown adipocytes immunostained for cytochrome c oxidase subunit 4 (COX4). Bright-field image was used to identify LDs, and TOM20 immunostaining was used to mark the mitochondrial network. White dashed circles denote LDs, white N denotes the nucleus, and white square denotes zoomed region.

(G) Quantification of COX4 distribution in brown adipocyte mitochondria. 490 mitochondria were assessed in total. $n = 22$ cells collected in 3 independent experiments.

(H) Brown adipocytes immunostained for ATP synthase. Bright-field image was used to identify LDs, and TOM20 immunostaining was used to mark the mitochondrial network. White dashed circles denote LDs, white N denotes the nucleus, and white square denotes zoomed region.

(I) Quantification of ATP synthase distribution in brown adipocyte mitochondria. 507 mitochondria were assessed in total. $n = 20$ cells collected in 4 independent experiments.

Data are expressed as means \pm SEM. * $p < 0.05$, *** $p < 0.0001$.

See also [Figure S2](#).

western blot analysis of the average protein expression of isolated CM and PDM.

Peridroplet Mitochondria Have Lower Fatty Acid Oxidation Capacity but Increased TCA Cycle Capacity

Our results show that PDM have enhanced OXPHOS protein levels and respiratory capacity. However, these results were not

sufficient to determine whether PDM have a preference for fuel oxidation by β -oxidation or through the TCA cycle. If PDM are specialized for fat oxidation, we reasoned that (1) isolated PDM will have enhanced fatty acid oxidation capacity, (2) PDM will have enhanced levels of uncoupling protein 1 (UCP1), and (3) mitochondrial contact with LDs will be increased during cold-induced thermogenesis when fatty acid oxidation rate is maximal.

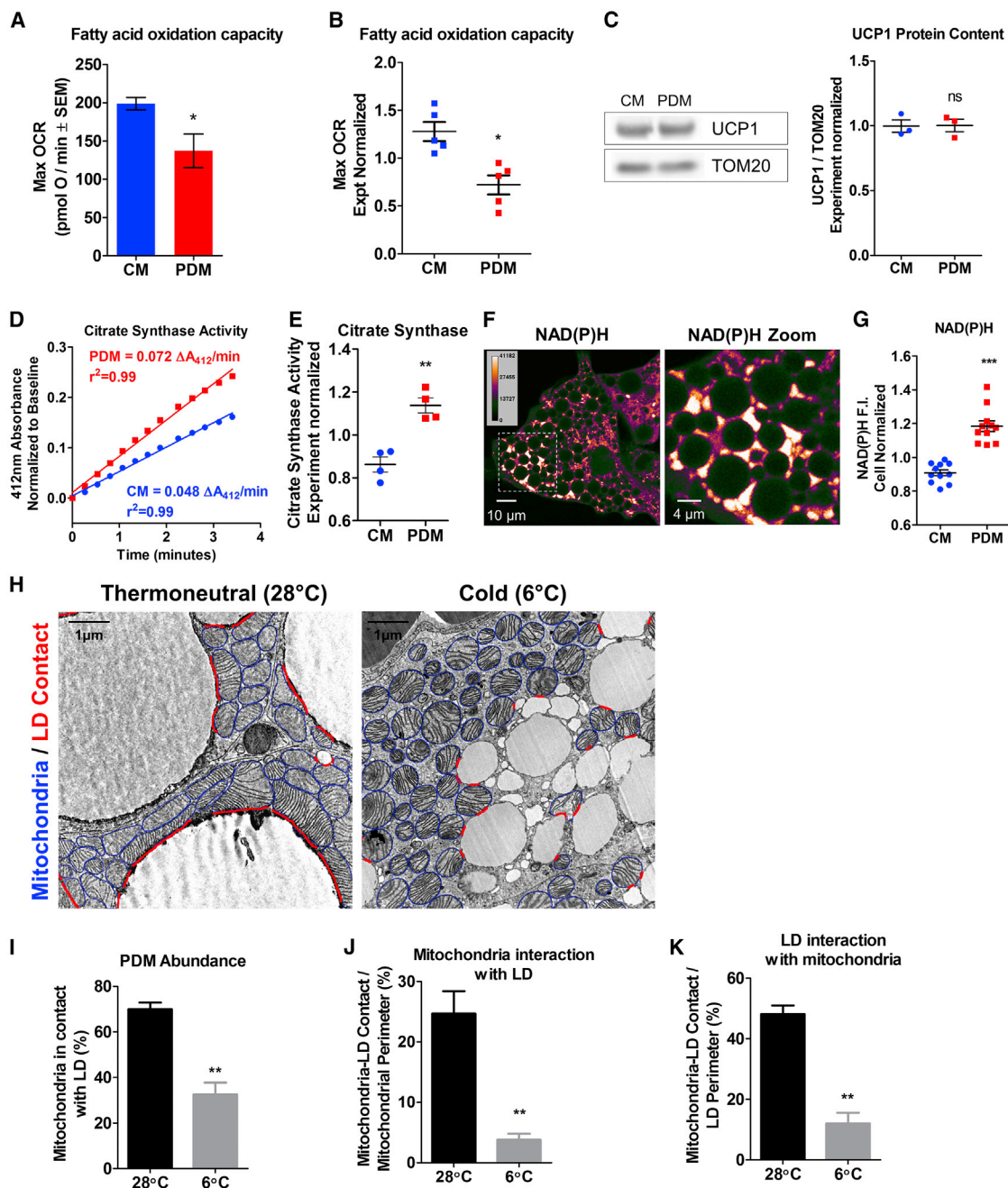


Figure 4. Peridroplet Mitochondria Have Decreased Fatty Acid Oxidation Capacity, and Mitochondria-LD Contact Is Decreased upon Activation of Thermogenic Fatty Acid Oxidation *In Vivo*

(A) PDM have lower fatty acid oxidation capacity. Representative quantification of maximal palmitoyl-carnitine-driven oxygen consumption rate (max OCR) in isolated peridroplet (PDM) and cytoplasmic (CM) mitochondria. 4–6 technical replicates per group.

(B) Quantification of palmitoyl-carnitine oxidation capacity. $n = 5$ independent experiments. For each individual experiment, average OCR values of CM and PDM were normalized to the average OCR of total mitochondria (see [Quantification and Statistical Analysis](#) for full equations).

(C) UCP1 protein is similarly abundant in PDM and CM. Western blot analysis of UCP1 in CM and PDM. $n = 3$ independent mitochondrial isolations. Data were normalized as in (B).

(D and E) PDM have higher activity of the TCA cycle enzyme citrate synthase.

(D) Representative traces of citrate synthase DTNB absorbance assay in isolated mitochondria normalized to baseline. Citrate synthase activity was determined for CM and PDM by the rate of absorbance gain.

(E) Quantification of citrate synthase specific activity. $n = 4$ independent mitochondrial isolations. Data were normalized as in (B).

(F and G) PDM have increased NAD(P)H content.

(legend continued on next page)

To test these predictions, we measured fatty acid-driven respiration and UCP1 content in isolated mitochondria. Contrary to our prediction, maximal respiration driven by palmitoyl-carnitine was significantly lower in PDM compared to CM (Figures 4A and 4B). We confirmed that PDM have reduced fatty acid oxidation capacity by normalizing fat oxidation capacity to pyruvate oxidation capacity assayed in parallel wells on the same Seahorse XF96 plate (Figure S3). Furthermore, western blot analysis showed no difference in UCP1 levels (Figure 4C), suggesting that PDM are not specialized for thermogenic fat oxidation.

Since mitochondrial β -oxidation and TCA flux are two competing pathways (Garland et al., 1968), we next tested whether enhanced PDM respiratory capacity is supported by higher capacity for TCA cycling. To this end, we determined the activity of the TCA enzyme citrate synthase (CS) by 5,5'-dithio-bis(2-nitrobenzoic acid) (DTNB) absorbance assay. DTNB reduction rate was $33.1\% \pm 9.7\%$ higher in isolated PDM compared to CM (Figures 4D and 4E), suggesting higher TCA cycle capacity. We next measured NAD(P)H levels in cultured primary brown adipocytes using live-cell fluorescence microscopy. NAD(P)H levels as measured by 450 nm emission were $30.8\% \pm 3.5\%$ higher in PDM compared to CM (Figures 4F and 4G), consistent with CS measurements (Figures 4D and 4E). Taken together, these results suggest that enhanced ATP synthesis and electron transport capacity in PDM are supported by increased substrate oxidation through the TCA cycle.

Mitochondria-LD Contact Is Decreased upon Activation of Thermogenic Fatty Acid Oxidation *In Vivo*

The reduced fatty acid oxidation capacity observed in isolated PDM suggested that PDM are not specialized for fat oxidation. To determine the relation between PDM and fatty acid oxidation *in vivo*, we next assessed mitochondria-LD contact in BAT harvested from cold-adapted animals, in which fatty acid oxidation is maximized to produce heat. If PDM play a significant role in fatty acid oxidation, we predicted that mitochondria-LD contact will be increased in cold-exposed mice compared to mice adapted to thermoneutral conditions, where fatty acids are stored in LDs. Contrary to our predictions, the number of mitochondria in contact with LDs was more than 50% lower in cold-exposed mice compared to thermoneutral conditions (Figures 4H and 4I). Quantitative image analysis confirmed this: mitochondria-LD contact area represented only $3.8\% \pm 1.0\%$ of mitochondrial perimeter in cold-exposed mice compared to $24.7\% \pm 3.7\%$ in thermoneutral conditions (Figure 4J). To control for reduced LD surface area resulting from lipid oxidation during cold exposure, we quantified mitochondria-LD contact area as a proportion of LD perimeter (Figure 4K). Mitochondria-LD contact

as a proportion of LD surface was reduced by more than 75% in cold-exposed animals, confirming that mitochondria-LD contact is reduced by cold exposure. These results suggest that mitochondria-LD contact is negatively associated with fatty acid oxidation *in vivo*.

Mitochondria-Lipid Droplet Association Promotes Lipid Droplet Expansion

The high level of mitochondria-LD contact observed in thermoneutral conditions led us to hypothesize that mitochondria-LD contact plays a role in LD expansion rather than oxidation. To test this, we sought to create an experimental system in which mitochondrial association to LDs can be induced. Perilipin5 (Plin5) is a LD-coating protein that is uniquely capable of recruiting mitochondria to LDs (Bosma et al., 2012; Wang et al., 2013) through its C-terminal region (Figure 5A) (Wang et al., 2011). We therefore assessed the effect of adenovirus-mediated Plin5 overexpression on LD expansion in cultured brown adipocytes.

To determine mitochondrial association to LDs, we stained transduced cells with TMRE to label the mitochondrial network and BODIPY 493/503 (BODIPY) to label LDs. Confocal microscopy revealed that brown adipocytes expressing the full version of Plin5 that includes its mitochondrial recruiting sequence (Plin5) significantly increased mitochondrial recruitment to LDs relative to untransduced control cells (Figures 5B and 5C). We confirmed that the mitochondrial recruitment phenotype was not due to increased LD content as areas of the cytoplasm remained free of LDs and mitochondria in brown adipocytes overexpressing Plin5 (Figure S4A).

To control for Plin5 effects that are not related to mitochondrial recruitment, we overexpressed a truncated version of Plin5 that lacks the C-terminal mitochondrial recruiting sequence (Plin5 Δ 399–463). Confocal imaging confirmed that Plin5 Δ 399–463 did not significantly increase mitochondrial recruitment to LDs relative to untransduced control brown adipocytes (Figures 5B and 5C). Next, to determine the effect of Plin5-mediated mitochondrial recruitment to LDs on bioenergetic capacity, we performed respirometry on intact transduced cells. Brown adipocytes expressing the full version of Plin5 that contains the mitochondrial recruiting sequence had $83.2\% \pm 24.0\%$ higher ATP-linked respiration and $54.1\% \pm 28.6\%$ higher spare respiratory capacity compared to brown adipocytes expressing truncated Plin5 Δ 399–463 that lacks the mitochondrial recruiting sequence independent of mitochondrial mass (Figures S4B–S4E). These results confirmed that mitochondrial recruitment to LDs by Plin5 promotes increased respiratory capacity, in agreement with data from isolated PDM (Figures 2C–2E).

(F) Confocal image of NAD(P)H fluorescence in living cultured brown adipocytes. Image was pseudo-colored for quantitative display (see calibration bar in top left). Note the high level of NAD(P)H in PDM.

(G) Quantification of NAD(P)H level. $n = 24$ cells imaged in 6 independent experiments. CM and PDM fluorescent intensities (F.I.) were normalized to average cell F.I. for each individual cell.

(H) Electron micrographs (EMs) of BAT harvested from mice adapted to thermoneutral conditions (28°C), where fatty acids are stored in lipid droplets, and cold environment (6°C), where thermogenic fatty acid oxidation is robustly increased. Blue lines highlight mitochondrial perimeter, and red lines highlight overlap between mitochondria and LD border.

(I–K) Mitochondria in contact with lipid droplets were quantified by count (I), % mitochondrial perimeter (J), and % lipid droplet perimeter (K). $n = 10$ EMs per condition.

Data are expressed as means \pm SEM. ns $p > 0.05$, * $p < 0.05$, ** $p < 0.001$, *** $p < 0.0001$.

See also Figure S3.

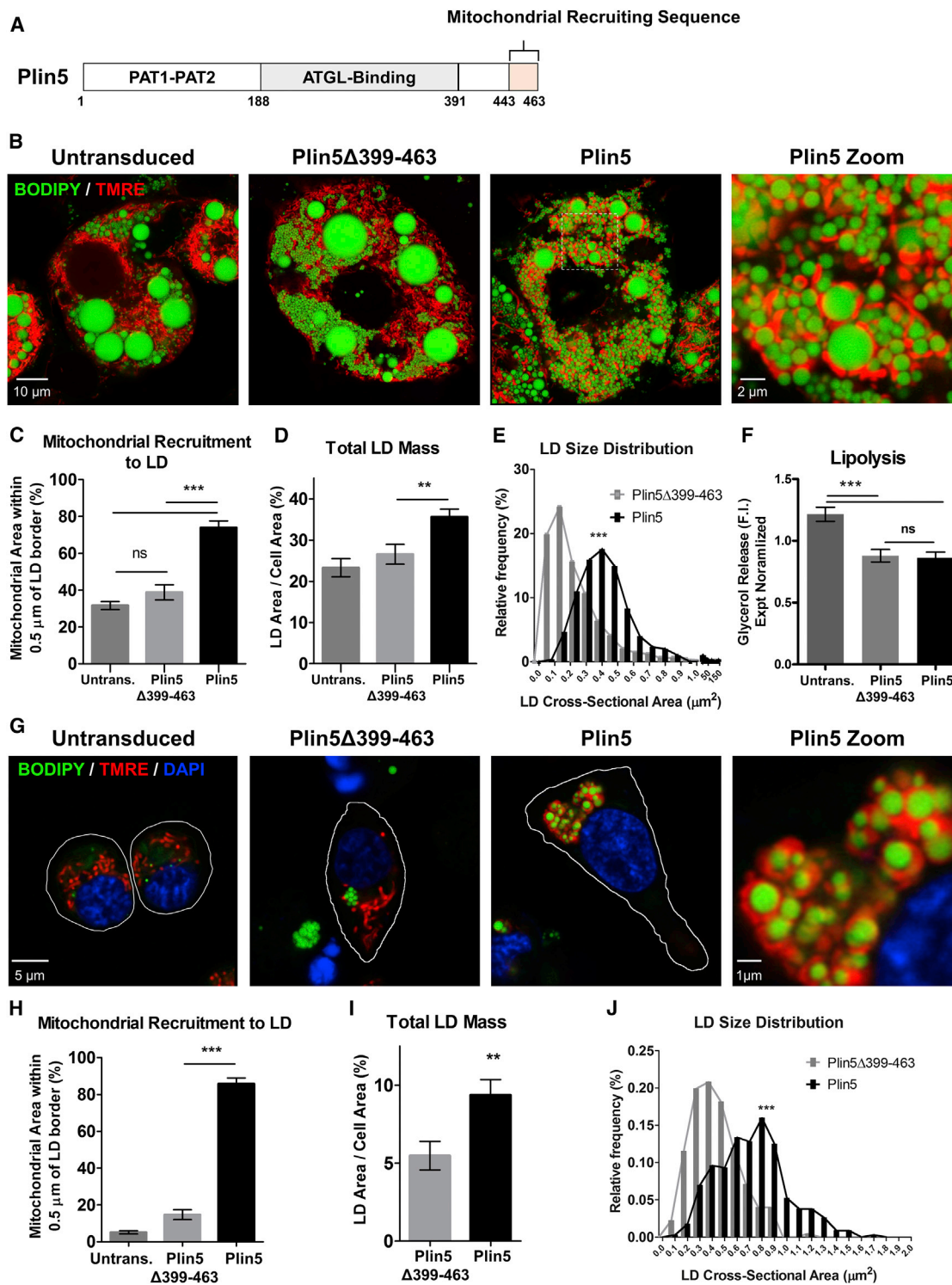


Figure 5. Mitochondria-Lipid Droplet Association Promotes Lipid Droplet Expansion

(A) Schematic representation of Perilipin5 (Plin5) domains: the conserved perilipin domains PAT1 and PAT2, the ATGL-binding domain responsible for lipolysis regulation, and the mitochondrial recruiting sequence.

(B) Super-resolution confocal images of living brown adipocytes untransduced (control), transduced with the full-length Plin5 that contains mitochondrial recruiting sequence (Plin5), and transduced with truncated Plin5 that lacks the mitochondrial recruitment sequence (Plin5 Δ 399-463). Mitochondria are marked by TMRE staining and lipid droplets (LDs) by BODIPY 493/503. Note the increased LD mass and mitochondrial recruitment in Plin5-transduced cells.

(C) Quantification of mitochondrial recruitment to LDs assessed as the area of mitochondria within 0.5 μ m of LD border. $n = 14$ –24 brown adipocytes analyzed per group from 4 independent experiments.

(legend continued on next page)

Next, to determine the effect of mitochondrial recruitment on lipid accumulation, we quantified LD area in confocal microscopy images. Quantitative image analysis revealed that brown adipocytes expressing the full version of Plin5 that contains mitochondrial recruiting sequence (Plin5) had significantly higher LD accumulation (Figure 5D) and size (Figure 5E) compared to cells expressing the truncated version of Plin5 that lacks the mitochondrial recruiting sequence (Plin5 Δ 399–463). We confirmed that these effects were not related to lipolysis regulation as overexpression of Plin5 and Plin5 Δ 399–463 reduced lipolysis to the same extent (Figure 5F). These results suggest that mitochondrial association to LDs promotes LD expansion independent of lipolysis regulation.

To determine whether this phenomenon is unique to brown adipocytes, we repeated this experimental series in INS1, a pancreatic β cell line with low levels of endogenous Plin5 expression and lipogenic capacity (Figure 5G). Consistent with brown adipocytes, more than 80% of mitochondria were recruited to LDs in INS1 cells expressing Plin5 compared to less than 12% in Plin5 Δ 399–463 (Figure 5H), with large areas of the cytoplasm without LD and mitochondria in INS1 cells expressing Plin5 (Figure 5G). Furthermore, LD accumulation and size were significantly higher in INS1 cells expressing Plin5 compared to Plin5 Δ 399–463 (Figures 5I and 5J). These results suggest that mitochondrial contact with LDs promotes the expansion of LDs in non-adipose cell types.

Mitochondria-Lipid Droplet Association Promotes Triacylglyceride Synthesis

We reasoned that mitochondrial recruitment to LDs can expand LDs by enhancing the synthesis of TAGs. To test this, we assessed the effect of Plin5 overexpression on TAG synthesis. As before, we performed parallel experiments in brown adipocytes expressing truncated Plin5 Δ 399–463 that lacks mitochondrial recruiting sequence but preserves lipolysis regulatory function. Brown adipocytes were incubated with BODIPY C12 558/568 (C12), a fluorophore-conjugated fatty acid, and thin-layer chromatography (TLC) was used to resolve cellular lipid species (Rambold et al., 2015). Plin5 increased C12 incorporation into TAG by 52.1% \pm 14.3% while Plin5 Δ 399–463 increased C12 incorporation by only 11.0% \pm 2.5% relative to untransduced controls (Figures 6A and 6B). To confirm that C12 incorporation was dependent on TAG synthesis, we incubated brown adipocytes with Triacsin C, a potent inhibitor of fatty acid esterification into TAG (Figures 6C and 6D). Triacsin C decreased C12 incor-

poration into TAG by 43.5% and increased free C12 by 28.6%, confirming that C12 incorporation into TAG depends on esterification.

We reasoned that LD recruitment could promote TAG synthesis by fulfilling the energy requirements of ATP-dependent TAG synthesis reactions (Mashek et al., 2007; Prentki and Madiraju, 2012). To test this, we assessed the effect of the mitochondrial ATP synthase inhibitor oligomycin A on Plin5-enhanced TAG synthesis. C12 incorporation in Plin5-expressing cells was 17.8% \pm 3.6% more sensitive to oligomycin inhibition compared to Plin5 Δ 399–463 and untransduced controls (Figures 6E and 6F). These results suggest that mitochondrial association to LDs enhances TAG synthesis in an OXPHOS-dependent manner.

Peridroplet Mitochondria Have Unique Structure, Fusion Dynamics, and Movement

Mitochondria are highly dynamic organelles that continuously undergo cycles of fusion and fission to regulate network morphology and distribute network content (Chen et al., 2005; Liesa and Shirihai, 2013; Nakada et al., 2001). We therefore hypothesized that PDM maintain unique functional and proteomic identity through distinct fusion-fission dynamics. To test this, we first assessed the morphology of PDM and CM in EMs of mice adapted to thermoneutrality, where PDM are the most abundant. Mitochondria with direct contact to LDs had a 93.2% \pm 22.9% larger cross-sectional area and a 47.4% \pm 7.3% longer aspect ratio compared to mitochondria with no visible LD association (Figures 7A–7C). Analysis of internal mitochondrial structure also revealed that cristae in mitochondria associated with LDs were arranged in perpendicular orientation to the axis of mitochondria-LD interface and were 12.0% \pm 0.9% shorter and 5.4% \pm 0.8% wider compared to mitochondria with no visible association to LDs (Figures S5A–S5C). To determine whether PDM structural specializations are preserved in cultured cells, we performed confocal microscopy in living brown adipocytes transduced with mitochondrially targeted photo-activatable GFP (mtPAGFP). Transduced brown adipocytes were stained with TMRE to visualize the entire mitochondrial network. Individual mitochondria were photo-converted by two-photon laser pulse and imaged immediately thereafter (Figure 7D). Quantitative image analysis confirmed that PDM are more elongated than CM in cultured cells (Figure 7E). Taken together, these results suggest that PDM functional specialization is matched by specialized structure.

(D) Quantification of LD mass by cross-sectional area of BODIPY 493/503 normalized to cell area. $n = 17$ –33 brown adipocytes per group from 4 independent experiments.

(E) LD size distribution assessed by cross-sectional area of individual LDs. $n = 302$ –489 LDs per group from 4 independent experiments.

(F) Quantification of lipolysis by glycerol release assay. $n = 3$ independent experiments. For each individual experiment, average values of CM and PDM were normalized to the average values of total mitochondria (see Quantification and Statistical Analysis for full equations).

(G) Super-resolution confocal images of living INS1 pancreatic β cell line untransduced (control), transduced with Plin5 and Plin5 Δ 399–463, and stained with TMRE to mark mitochondria and BODIPY 493/503 to mark LDs. White line delineates cell border. Note the increased LD mass and mitochondrial recruitment in Plin5.

(H) Quantification of mitochondrial recruitment to LDs assessed as the area of mitochondria within 0.5 μ m of LD border. $n = 12$ –20 INS1 cells analyzed per group from 3 independent experiments.

(I) Quantification of LD mass by cross-sectional area of BODIPY 493/503 normalized to cell area. $n = 13$ –19 INS1 cells per group from 3 independent experiments.

(J) LD size distribution assessed by cross-sectional area of individual LDs. $n = 226$ –344 LDs per group from 3 independent experiments.

Data are expressed as means \pm SEM. ns $p > 0.05$, * $p < 0.05$, ** $p < 0.001$, *** $p < 0.0001$.

See also Figure S4.

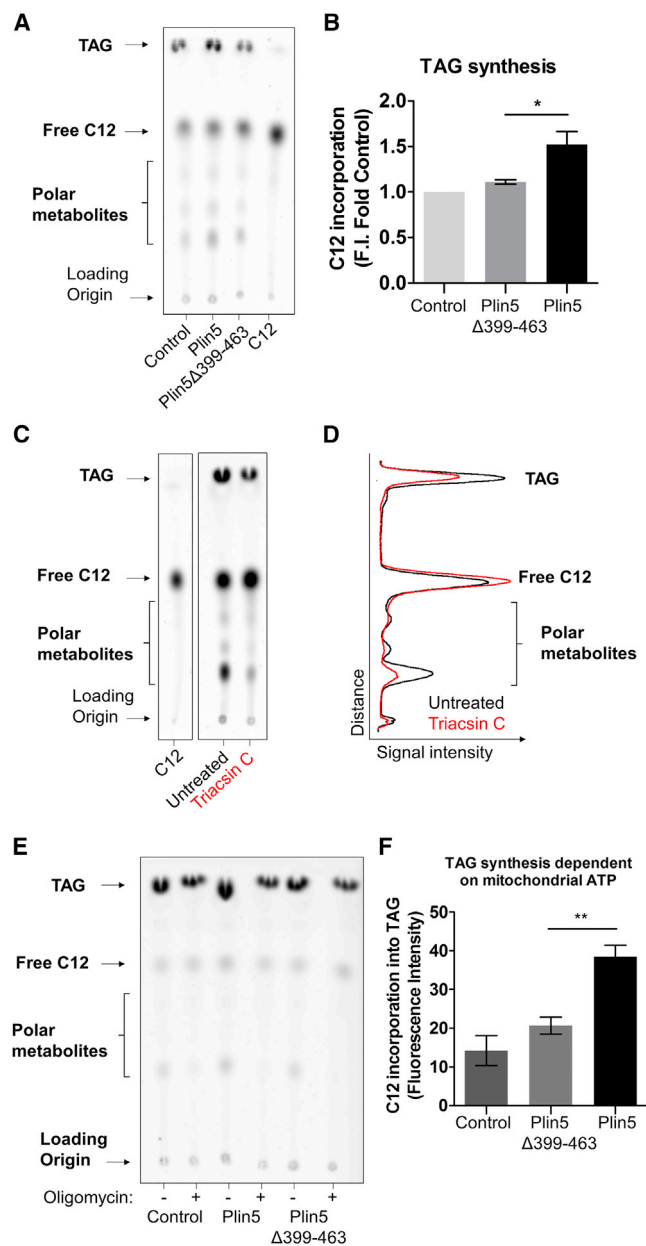


Figure 6. Mitochondria-Lipid Droplet Association Promotes Triacylglyceride Synthesis

(A) Representative thin-layer chromatography (TLC) of cellular lipids extracted from cultured brown adipocytes untransduced (control), transduced with the full-length Plin5 that contains mitochondrial recruiting sequence (Plin5), and transduced with truncated Plin5 that lacks the mitochondria recruitment sequence (Plin5 Δ 399-463). Cells were incubated with BODIPY C12 558/568 (C12) overnight to assess triacylglyceride (TAG) synthesis. The mobility of fatty acid species from loading origin is determined by relative polarity, with TAG migrating the highest.

(B) Quantification of TAG from $n = 3$ independent experiments. Data were normalized to control for each individual experiment.

(C and D) TLC of cultured brown adipocytes incubated with C12 with or without the fatty acid esterification inhibitor Triacsin C (red) (C). In the histogram, note the decrease in TAG and increase in free C12 induced by Triacsin C (D).

(E) Representative TLC of cultured brown adipocytes incubated with C12 with or without the mitochondrial ATP synthase inhibitor oligomycin.

We next assessed the fusion activity of CM and PDM in cultured brown adipocytes using mtPAGFP. The dilution of mtPAGFP fluorescence intensity over time reflects fusion of photo-activated mitochondria with non-photo-activated mitochondria. A $150 \mu\text{m}^2$ region of the cell containing primarily PDM or CM was photo-converted by two-photon laser pulse and imaged continuously at 15 min intervals. The mtPAGFP dilution rate was significantly slower in PDM compared to CM (Figures 7F and 7G), suggesting that PDM have reduced fusion compared to CM and decreased content exchange with the rest of the mitochondrial network.

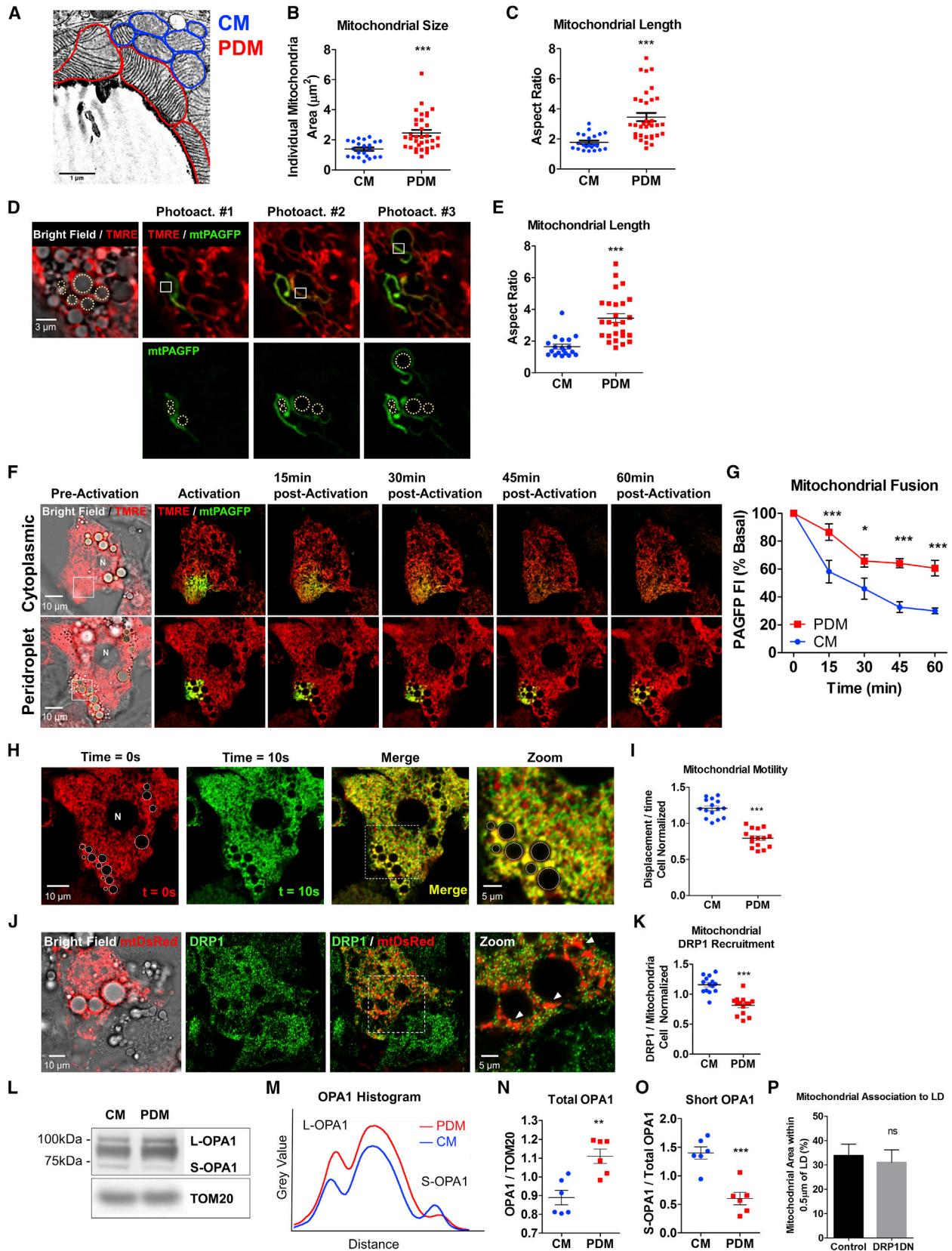
We reasoned that reduced PDM fusion could result from a reduction in one or more of the determinants of fusion: (1) mitofusin (Mfn) expression, (2) mitochondrial membrane potential (MMP), and (3) mitochondrial motility (Twig et al., 2010). Western blot analysis ruled out Mfn expression as the cause of reduced fusion as Mfn2 expression was high in PDM relative to CM (Figures S5D and S5E). Additionally, MMP analysis using the membrane potential-sensitive dye TMRE showed that PDM do not have reduced MMP (Figures S5F and S5G). To determine whether LD association reduces fusion by decreasing mitochondrial motility, we next quantified mitochondrial displacement over time in time-lapse confocal imaging. PDM displacement rate was significantly lower compared to CM (Figures 7H and 7I), suggesting that LD anchoring reduces PDM fusion by arresting motility. Taken together, these results suggest that PDM have reduced mitochondrial motility leading to decreased fusion activity that promotes their segregation from CM.

Peridroplet Mitochondria Have Reduced DRP1 Recruitment and OPA1 Processing

The concomitant reduction in PDM fusion activity and marked elongation led us to hypothesize that reduced fusion rate is matched by reduced fission activity (Chen et al., 2003). To assess outer membrane fission, we measured the recruitment of DRP1 to mitochondria by immunofluorescence (Cereghetti et al., 2008). DRP1 was immunolabeled in cultured cells where the mitochondrial network was labeled by mitochondrially targeted DsRed (mtDsRed). Confocal imaging revealed significantly lower DRP1 staining on PDM compared to CM (Figures 7J and 7K), suggesting lower outer membrane fission activity. Next, to assess inner membrane fission, we measured OPA1 processing in isolated mitochondria. Proteolytic cleavage of the long-form OPA1 (L-OPA1) to short OPA1 (S-OPA1) is associated with inner membrane fission (Anand et al., 2014). Western blot analysis revealed significantly lower levels of S-OPA1 in PDM compared to CM, suggesting lower inner membrane fission activity (Figures 7L–7O). We reasoned that fission arrest can be a cause or a consequence of LD recruitment. To test this, we assessed mitochondrial LD association in cells expressing the dominant-negative DRP1 K38A (DRP1DN) (Smirnova et al., 2001). DRP1DN did not enhance mitochondrial recruitment to

(F) Quantification of TAG synthesis dependent on mitochondrial ATP synthase activity from $n = 3$ independent experiments. OXPHOS-dependent TAG synthesis was calculated as the difference in TAG between oligomycin-treated and untreated cells.

Data are expressed as means \pm SEM. * $p < 0.05$, ** $p < 0.001$.



(legend on next page)

LDs (Figures 7P; S5H), suggesting that fission arrest is a consequence rather than a cause of LD recruitment. Taken together, these results suggest that LD association reduces fission protein recruitment and processing that promotes PDM elongation.

DISCUSSION

Peridroplet Mitochondrial Isolation by Differential Centrifugation

In this study, we developed an approach to isolate intact respiring PDM and determine their bioenergetic function for the first time. Our approach took advantage of the buoyancy of LDs to separate LD-bound PDM from CM. PDM were then purified using high-speed centrifugation, a procedure previously shown to strip LD-associated proteins (Figure 1) (Ding et al., 2013; Yu et al., 2015). These results raise important considerations for the interpretation of past and future experiments with isolated mitochondria. First, mitochondrial isolation protocols that eliminate lipid fraction by aspiration (Rogers et al., 2011) and/or gauze filtration (Cannon and Nedergaard, 2001a) may miss physiologically relevant changes that occur in PDM, but not in CM. Second, isolation protocols that include an initial high-speed centrifugation step prior to low-speed centrifugation steps (Cannon and Nedergaard, 2001a; Djafarzadeh and Jakob, 2017) may inadvertently strip LDs, resulting in a mixed population of CM and PDM. To our knowledge, this is the first report to specifically isolate intact respiring PDM from any tissue type and directly determine their functional role.

PDM Have Specialized Oxidative Phosphorylation Protein Composition and Capacity

BAT mitochondria isolated by previous methods were shown to have low levels of ATP synthase elementary particles (Lindberg et al., 1967) and activity (Cannon and Vogel, 1977). Our study reveals that PDM have more than 2-fold higher ATP synthesis capacity matched by enriched ATP synthase protein subunits when compared to CM, which may explain the relatively low levels of ATP synthesis reported in mitochondria isolated from BAT using previous methods. Consistent with higher ATP synthesis capacity, PDM were also enriched with COX protein and had increased electron transport capacity (Figures 2 and 3). We confirmed that higher respiration was not due to an artifactual difference in mitochondrial enrichment of PDM fraction by mass spectrometry analysis (Figure 1H) and imaging of mitochondria loaded within Seahorse XF96 plates (Figures 2A and 2B). In addition, careful attention was dedicated to eliminating potential artifacts due to the presence of free fatty acids. Free fatty acids can alter respiration by (1) providing fuel for β -oxidation, (2) acting as weak uncouplers (Li et al., 2014), and (3) activating UCP1 (Fedorenko et al., 2012). To address this, we assessed the lipid contents of CM and PDM (Figures 1F and 1G) and supplemented the respiratory buffer with bovine serum albumin (BSA) to remove free fatty acids from solution as well as the UCP1 inhibitor GDP. ADP- and FCCP-stimulated respiration confirmed that mitochondria were coupled at the start of the assay. Free fatty acids could not serve as mitochondrial fuels in this system

Figure 7. Peridroplet Mitochondria Have Unique Structure, Fusion-Fission Dynamics, and Motility

(A–C) Electron micrograph (EM) of BAT (A) and quantification of mitochondrial size (B) and length (C). Analysis was performed in BAT harvested from mice adapted to thermoneutral conditions (28°C), where peridroplet mitochondria (PDM) are most abundant. Red lines highlight PDM, and blue lines highlight cytoplasmic mitochondria (CM). Note the elongation of PDM. Mitochondrial size and shape were quantified in $n = 22$ –34 mitochondria from 10 EMs per group. (D and E) Confocal microscopy of living cultured brown adipocytes. (D) Confocal images of brown adipocytes transduced with mitochondrially targeted photo-activatable GFP (mtPAGFP) stained with TMRE to label the mitochondrial network. mtPAGFP in single mitochondria (white squares) were sequentially photo-converted and imaged immediately. Yellow circles denote lipid droplets. (E) Quantification of mitochondrial shape as delineated by mtPAGFP. $n = 47$ mitochondria from 4 independent imaging experiments. (F and G) Mitochondrial fusion assay images (F) and quantification (G) in living cultured brown adipocytes. Brown adipocytes transduced with mtPAGFP were stained with TMRE to label the mitochondrial network. Yellow dashed circles denote LDs, and white N denotes the nucleus. mtPAGFP was photo-converted in a small region of the cell (white squares) and its fluorescence intensity tracked over time. The dilution of mtPAGFP fluorescence intensity over time results from fusion between activated mitochondria with non-activated mitochondria. $n = 5$ cells per group imaged in 3 independent experiments. Data were normalized to baseline and statistically analyzed by two-way ANOVA for repeated measures with Bonferroni post-test. (H and I) PDM have reduced motility compared to CM. (H) Pseudo-colored confocal images of brown adipocyte at two different time points (red and green). Merged image of two time points reveals immobile mitochondria (yellow) and mobile mitochondria that change position over time (red and green). White dashed circles denote LDs, white N denotes the nucleus, and white dashed square denotes zoomed region. Note the reduced mobility of PDM compared to CM. (I) Quantification of mitochondrial motility. Mitochondrial motility was quantified in time-lapse images as the percent of area displaced over a period of 10 s. For each individual cell, CM and PDM motility values were normalized to the average motility value of all mitochondria in the cell. $n = 15$ cells imaged in 3 independent experiments. (J) Confocal image of fixed cultured brown adipocytes immunolabeled for the mitochondrial fission protein DRP1. LDs were identified by bright-field images, and the mitochondrial network was marked with mitochondrially targeted DsRed (mtDsRed). Note the low levels of DRP1 recruitment to PDM (white arrows). (K) Quantification of DRP1 associated with CM and PDM. DRP1 association was quantified as puncta area divided by mitochondrial area. In each individual cell, DRP1 association to CM and PDM values were normalized to the average of the entire cell. $n = 14$ cells per group imaged in 3 independent experiments. (L–O) Western blot analysis of the mitochondrial inner membrane protein OPA1 in isolated PDM and CM. (L and M) Western blot probed with OPA1 (L) and histogram (M). Proteolytic cleavage of the long-form OPA1 (L-OPA1) to short-OPA1 (S-OPA1) is associated with inner membrane fission. Densitometry of L-OPA1 and S-OPA1 in PDM and CM is shown in representative histogram. (N and O) Quantification of total OPA1 (N) and S-OPA1 (O) in CM and PDM. $n = 6$ –7 independent mitochondrial isolations. (P) Fission arrest by DRP1 dominant-negative (DRP1DN) expression does not recruit mitochondria to LD surface compared to transduction control. Mitochondrial recruitment was assessed as the area of mitochondria within 0.5 μm of LD border. $n = 10$ cells analyzed per group. Data are expressed as means \pm SEM. ns $p > 0.05$, * $p < 0.05$, ** $p < 0.001$, *** $p < 0.0001$. See also Figure S5.

because the enzymes and cofactors required for acyl-CoA and acyl-carnitine syntheses are not present in assay buffer. Our results thus demonstrate that PDM represent a mitochondrial subpopulation with distinct bioenergetics and protein composition.

Peridroplet Mitochondria Are Segregated by Reduced Fusion-Fission Dynamics

In every cell type in which mitochondrial dynamics has been studied, mitochondria were shown to go through continuous cycles of fusion and fission that equilibrate the mitochondrial content across the mitochondrial population of the cell. We have previously reported that mitochondria in brown adipocytes continuously engage in fusion and fission activities (Wikstrom et al., 2014). The mechanism by which mitochondrial subpopulations can maintain separate function and composition in brown adipocytes was therefore unclear. Disparate mitochondrial subpopulations have been previously observed in tissues in which mitochondrial subpopulations are separated in space (Wikstrom et al., 2009). For example, in striated muscle, it has been observed that subsarcolemmal mitochondria that are separated from interfibrillar mitochondria by the sarcomere have specialized form and function (Palmer et al., 1977). However, the brown adipocyte lacks the cytoplasmic subdivision that is mediated by myocyte sarcomeres, and thus, one expects fusion and fission to continuously equilibrate mitochondrial content across the adipocyte mitochondrial population (Wikstrom et al., 2014). Our results demonstrate that PDM have reduced fusion-fission dynamics that segregate them from the rest of the mitochondrial population (Figures 7F and 7G). Various evidences support that altered mitochondrial dynamics are a consequence rather than a cause of LD recruitment: (1) neither fusion arrest (Boutant et al., 2017) nor fission arrest (Figure 7P) recruits mitochondria to LDs and (2) mitochondrial recruitment to LDs by Plin5 promotes mitochondrial elongation (Wang et al., 2013). This supports the conclusion that reduced mitochondrial dynamics are a consequence rather than a cause of LD association. Furthermore, our observation that PDM are stationary (Figures 7H and 7I) suggests a mechanism by which LD association reduces mitochondrial dynamics, as we have previously shown that stationary mitochondria have markedly lower probability to undergo fusion (Twig et al., 2008, 2010). Our results thus suggest that PDM maintain functional and proteomic segregation from CM by having reduced motility and fusion-fission dynamics.

Peridroplet Mitochondria Are Not Associated with Fatty Acid Oxidation

Recent studies have hypothesized that PDM facilitate fatty acid trafficking toward mitochondrial β -oxidation (Boutant et al., 2017; Rambold et al., 2015), while others have suggested that mitochondria-LD association enhances LD biogenesis and thereby protects mitochondria from lipotoxicity (Nguyen et al., 2017; Stone et al., 2009; Wang et al., 2011). In this study, we employed BAT, a system that robustly shifts from LD expansion under thermoneutral conditions to lipid oxidation under cold/adrenergic stimulus. If PDM facilitate fat oxidation, we reasoned that mitochondria-LD association will increase during cold-induced thermogenesis when fatty acid oxidation rate is maximal. However, contrary to the hypothesis, mitochondrial association with

LDs was decreased by cold exposure (Figures 4H–4K). These results are consistent with the previously published observation that mitochondrial protein content is reduced in LDs isolated from BAT of cold-adapted mice compared to mice in thermoneutral environment (Yu et al., 2015). Our analyses of isolated mitochondria confirmed that PDM have lower fatty acid oxidation capacity and higher TCA cycle capacity compared to CM (Figures 4A–4G). Taken together, these results support the conclusion that PDM are not specialized for lipid oxidation in BAT.

Mitochondria-Lipid Droplet Interaction Enhances Lipid Droplet Expansion

The high level of mitochondria-LD contact observed in BAT under thermoneutral conditions led us to hypothesize that PDM play a role in LD expansion. To test this, we induced mitochondrial recruitment to LDs using adenoviral-mediated Plin5 overexpression, which has been shown to recruit mitochondria to LDs in multiple cell and tissue types (Bosma et al., 2012; Wang et al., 2011, 2013). Importantly, we developed a system in which the specific effects of mitochondrial recruitment can be differentiated from other Plin5 effects, such as lipolytic regulation. Our results show that mitochondrial recruitment to LDs doubled the size of LDs (Figure 5). Furthermore, the capacity of PDM to promote the incorporation of free fatty acids into TAG was dependent on mitochondrial ATP synthesis (Figure 6). This observation supports the conclusion that PDM enhance LD expansion by providing ATP to the ATP-demanding process of acyl-CoA synthesis and lipid cycling (Prentki and Madiraju, 2012). In addition, the increased TCA cycle capacity that we observed suggests that PDM may support LD expansion by providing citrate for *de novo* lipogenesis. Taken together, our results thus support the conclusion that PDM support LD expansion rather than oxidation.

We suggest that increased mitochondrial recruitment to LDs may be part of a generalized adaptive response in physiological conditions that require LD expansion, such as post-prandial lipid synthesis and storage. PDM-mediated LD expansion may also play a role in preventing muscle and liver injury from lipotoxicity in conditions of nutrient excess, such as obesity and hyperlipidemia. A better understanding of PDM and LD biology may therefore be important for developing new therapies for lipotoxic tissue injury and insulin resistance. Animal models in which mitochondria-LD association can be specifically modulated will be necessary to resolve such questions in future studies.

Limitations of Study

This study is the first to isolate intact respiring PDM and determine their unique composition and bioenergetics. However, our study has several limitations. Limitations of our PDM isolation approach include: (1) mitochondrial isolation by differential centrifugation results in relatively crude preparations contaminated with other organelles and cellular compartments. Mass spectrometry analysis of CM and PDM preparations revealed that approximately half of the proteins present in CM and PDM preparations were mitochondrial (Figure 1H), in agreement with previously published reports (Forner et al., 2009). (2) Mitochondrial isolation by differential centrifugation pools all PDM into a single pellet. As such, intermitochondrial heterogeneity (Figures

3F–3I) is lost in subsequent biochemical and functional assays, which may lead to underestimation of differences between CM and PDM populations (Figures 3A–3C). (3) PDM isolation by differential centrifugation may preferentially select for PDM attached to larger LDs with higher buoyancy. Small LDs with insufficient buoyancy could potentially contaminate the supernatant and CM pellet and lead to further underestimation of the differences between isolated CM and PDM properties. (4) Our method used high-speed centrifugation to strip PDM from LDs, a procedure that may alter their function; however, the close agreement between our proteomic and bioenergetic data in living cells and isolated mitochondria (Figures 2 and 3) suggests that isolated PDM preserved the metabolic phenotype observed in intact cells.

STAR★METHODS

Detailed methods are provided in the online version of this paper and include the following:

- **KEY RESOURCES TABLE**
- **CONTACT FOR REAGENT AND RESOURCE SHARING**
- **EXPERIMENTAL MODEL AND SUBJECT DETAILS**
 - Mice
 - Cell Culture
- **METHOD DETAILS**
 - Peridroplet Mitochondrial Isolation
 - Fluorescence Microscopy
 - Isolated Mitochondria Proteomics
 - Isolated Mitochondria Respirometry
 - Cytochrome c Oxidase Assay
 - ATP Synthesis Assay
 - Protein Gel Electrophoresis and Immunoblotting
 - Immunofluorescence
 - Citrate Synthase Assay
 - NADH Imaging
 - Electron Microscopy
 - Virus Preparation
 - Lipolysis Assay
 - Thin-Layer Chromatography
 - Mitochondrial Fusion Assay
- **QUANTIFICATION AND STATISTICAL ANALYSIS**

SUPPLEMENTAL INFORMATION

Supplemental Information includes five figures and can be found with this article online at <https://doi.org/10.1016/j.cmet.2018.03.003>.

ACKNOWLEDGMENTS

We would like to thank Carole Sztalyrd for guiding our lab into the field of PDM biology. We would like to thank Gilad Twig, Nathanael Miller, Kyle Trudeau, David Chess, and Michael Kirber for assistance with image acquisition and analysis. We would like to thank Anish Nag, Sarah Cohen, and Jennifer Lippincott-Schwartz for assistance with TLC and Aviva Joseph and Keith Luo for assistance with adenoviral generation. We would like to thank Pedro M. Quiros and Carlos López-Otin for assistance with brown adipocyte cell culture. We would like to thank Dr. Linsey Stiles, Dr. Dani Dagan, Dr. Evan Taddeo, Dr. Karel Erion, Dr. Ajit S. Divakaruni, Dr. Harold S. Sacks, Dr. Guy Las, Dr. Dovi Shlomo, Dr. Eleni Ritou, Dr. Nour Alsabeeh, Dr. Alicia Kowaltowski, Dr. Karen Reue, Dr. Andrea Havasi, Dr. Matthew Jones, Dr. José A. Enriquez, Dr. Susan

K. Fried, and Dr. Martin Picard for helpful discussions and advice. I.Y.B. was funded by T32-DK007201 Training Program in Metabolism, Endocrinology, and Obesity. O.S.S. is funded by NIH-NIDDK 5-R01DK099618-02. M.L. is funded by UCLA Department of Medicine Chair commitment and UCSD/UCLA Diabetes Research Center (DRC) grant (NIH P30 DK063491). M.F.O. was supported by the Conselho Nacional de Desenvolvimento Científico e Tecnológico (CNPq, <http://www.cnpq.br/>) grant #229526/2013-6. Additional support was provided by R01DK56690 (B.E.C. and O.S.S.), DK46220 (BNORC adipocyte and metabolic core), NIH R01 DK075017 (C.S.), and DK072488 (C.S.).

AUTHOR CONTRIBUTIONS

I.Y.B. wrote the manuscript, performed experiments and image analysis, and designed the study. O.S.S. and M.L. helped design the study and supervised manuscript writing. K.M. performed respirometry and NADH experiments and helped design the study. M.V. and A.P. performed Plin5 imaging and respirometry experiments. E.A. performed citrate synthase experiments. R.A.-P. performed cytochrome c oxidase experiments and helped optimize blue native PAGE and ATP synthase experiments. J.D.W. performed PAGFP and DRP1 image acquisition. S.C. performed electron microscopy processing and image acquisition. W.D.B. and J.A.W. performed mass spectrometry proteomics. B.E.C., M.S., M.F.O., C.S., and M.L. helped with experiments and data interpretation. All authors read and approved the final version of the manuscript.

DECLARATION OF INTERESTS

The authors declare that they have no conflict of interest.

Received: August 26, 2017

Revised: January 7, 2018

Accepted: March 13, 2018

Published: April 3, 2018

REFERENCES

- Anand, R., Wai, T., Baker, M.J., Kladt, N., Schauss, A.C., Rugarli, E., and Langer, T. (2014). The i-AAA protease YME1L and OMA1 cleave OPA1 to balance mitochondrial fusion and fission. *J. Cell Biol.* *204*, 919–929.
- Bosma, M., Minnaard, R., Sparks, L.M., Schaart, G., Losen, M., de Baets, M.H., Duimel, H., Kersten, S., Bickel, P.E., Schrauwen, P., and Hesselink, M.K. (2012). The lipid droplet coat protein perilipin 5 also localizes to muscle mitochondria. *Histochem. Cell Biol.* *137*, 205–216.
- Boutant, M., Kulkarni, S.S., Joffraud, M., Ratajczak, J., Valera-Alberni, M., Combe, R., Zorzano, A., and Cantó, C. (2017). Mfn2 is critical for brown adipose tissue thermogenic function. *EMBO J.* *36*, 1543–1558.
- Calvo, S.E., Clauser, K.R., and Mootha, V.K. (2016). MitoCarta2.0: an updated inventory of mammalian mitochondrial proteins. *Nucleic Acids Res.* *44* (D1), D1251–D1257.
- Cannon, B., and Nedergaard, J. (2001a). Respiratory and thermogenic capacities of cells and mitochondria from brown and white adipose tissue. *Methods Mol. Biol.* *155*, 295–303.
- Cannon, B., and Nedergaard, J. (2001b). Cultures of adipose precursor cells from brown adipose tissue and of clonal brown-adipocyte-like cell lines. *Methods Mol. Biol.* *155*, 213–224.
- Cannon, B., and Nedergaard, J. (2004). Brown adipose tissue: function and physiological significance. *Physiol. Rev.* *84*, 277–359.
- Cannon, B., and Vogel, G. (1977). The mitochondrial ATPase of brown adipose tissue. Purification and comparison with the mitochondrial ATPase from beef heart. *FEBS Lett.* *76*, 284–289.
- Cereghetti, G.M., Stangherlin, A., Martins de Brito, O., Chang, C.R., Blackstone, C., Bernardi, P., and Scorrano, L. (2008). Dephosphorylation by calcineurin regulates translocation of Drp1 to mitochondria. *Proc. Natl. Acad. Sci. USA* *105*, 15803–15808.
- Chen, H., Detmer, S.A., Ewald, A.J., Griffin, E.E., Fraser, S.E., and Chan, D.C. (2003). Mitofusins Mfn1 and Mfn2 coordinately regulate mitochondrial fusion and are essential for embryonic development. *J. Cell Biol.* *160*, 189–200.

- Chen, H., Chomyn, A., and Chan, D.C. (2005). Disruption of fusion results in mitochondrial heterogeneity and dysfunction. *J. Biol. Chem.* **280**, 26185–26192.
- Cinti, S., Cancellato, R., Zingaretti, M.C., Ceresi, E., De Matteis, R., Giordano, A., Himms-Hagen, J., and Ricquier, D. (2002). CL316,243 and cold stress induce heterogeneous expression of UCP1 mRNA and protein in rodent brown adipocytes. *J. Histochem. Cytochem.* **50**, 21–31.
- Cottet-Rousselle, C., Ronot, X., Leverve, X., and Mayol, J.-F. (2011). Cytometric assessment of mitochondria using fluorescent probes. *Cytometry A* **79**, 405–425.
- Ding, Y., Zhang, S., Yang, L., Na, H., Zhang, P., Zhang, H., Wang, Y., Chen, Y., Yu, J., Huo, C., et al. (2013). Isolating lipid droplets from multiple species. *Nat. Protoc.* **8**, 43–51.
- Divakaruni, A.S., Rogers, G.W., and Murphy, A.N. (2014). Measuring mitochondrial function in permeabilized cells using the Seahorse XF Analyzer or a Clark-type oxygen electrode. *Curr. Protoc. Toxicol.* **60**, 25.2.1–25.2.16.
- Djafarzadeh, S., and Jakob, S.M. (2017). Isolation of intact mitochondria from skeletal muscle by differential centrifugation for high-resolution respirometry measurements. *J. Vis. Exp.* <https://doi.org/10.3791/55251>.
- Fasshauer, M., Klein, J., Ueki, K., Kriaciuinas, K.M., Benito, M., White, M.F., and Kahn, C.R. (2000). Essential role of insulin receptor substrate-2 in insulin stimulation of Glut4 translocation and glucose uptake in brown adipocytes. *J. Biol. Chem.* **275**, 25494–25501.
- Fedorenko, A., Lishko, P.V., and Kirichok, Y. (2012). Mechanism of fatty acid-dependent UCP1 uncoupling in brown fat mitochondria. *Cell* **151**, 400–413.
- Forner, F., Kumar, C., Luber, C.A., Fromme, T., Klingenspor, M., and Mann, M. (2009). Proteome differences between brown and white fat mitochondria reveal specialized metabolic functions. *Cell Metab.* **10**, 324–335.
- Garland, P.B., Shepherd, D., Nicholls, D.G., and Ontko, J. (1968). Energy-dependent control of the tricarboxylic acid cycle by fatty acid oxidation in rat liver mitochondria. *Adv. Enzyme Regul.* **6**, 3–30.
- Huff, J., Bathe, W., Netz, R., Anhut, T., and Weisshart, K. (2015). The Airyscan Detector from ZEISS: Confocal Imaging with Improved Signal-to-Noise Ratio and Superresolution (Carl Zeiss Microscopy GmbH).
- Langousis, G., Shimogawa, M.M., Saada, E.A., Vashisht, A.A., Spreafico, R., Nager, A.R., Barshop, W.D., Nachury, M.V., Wohlschlegel, J.A., and Hill, K.L. (2016). Loss of the BBSome perturbs endocytic trafficking and disrupts virulence of *Trypanosoma brucei*. *Proc. Natl. Acad. Sci. USA* **113**, 632–637.
- Lapiente-Brun, E., Moreno-Loshuertos, R., Acín-Pérez, R., Latorre-Pellicer, A., Colás, C., Balsa, E., Perales-Clemente, E., Quirós, P.M., Calvo, E., Rodríguez-Hernández, M.A., et al. (2013). Supercomplex assembly determines electron flux in the mitochondrial electron transport chain. *Science* **340**, 1567–1570.
- Li, Y., Fromme, T., Schweizer, S., Schöttl, T., and Klingenspor, M. (2014). Taking control over intracellular fatty acid levels is essential for the analysis of thermogenic function in cultured primary brown and brite/beige adipocytes. *EMBO Rep.* **15**, 1069–1076.
- Liesa, M., and Shirihai, O.S. (2013). Mitochondrial dynamics in the regulation of nutrient utilization and energy expenditure. *Cell Metab.* **17**, 491–506.
- Lindberg, O., de Pierre, J., Rylander, E., and Afzelius, B.A. (1967). Studies of the mitochondrial energy-transfer system of brown adipose tissue. *J. Cell Biol.* **34**, 293–310.
- Mahdavian, K., Benador, I.Y., Su, S., Gharakhanian, R.A., Stiles, L., Trudeau, K.M., Cardamone, M., Enríquez-Zarralanga, V., Ritou, E., Aprahamian, T., et al. (2017). *Mfn2* deletion in brown adipose tissue protects from insulin resistance and impairs thermogenesis. *EMBO Rep.* **18**, 1123–1138.
- Mashek, D.G., Li, L.O., and Coleman, R.A. (2007). Long-chain acyl-CoA synthetases and fatty acid channeling. *Future Lipidol.* **2**, 465–476.
- Nakada, K., Inoue, K., Ono, T., Isobe, K., Ogura, A., Goto, Y.I., Nonaka, I., and Hayashi, J.I. (2001). Inter-mitochondrial complementation: Mitochondria-specific system preventing mice from expression of disease phenotypes by mutant mtDNA. *Nat. Med.* **7**, 934–940.
- Nguyen, T.B., Louie, S.M., Daniele, J.R., Tran, Q., Dillin, A., Zoncu, R., Nomura, D.K., and Olzmann, J.A. (2017). DGAT1-dependent lipid droplet biogenesis protects mitochondrial function during starvation-induced autophagy. *Dev. Cell* **42**, 9–21.e5.
- Palmer, J.W., Tandler, B., and Hoppel, C.L. (1977). Biochemical properties of subsarcolemmal and interfibrillar mitochondria isolated from rat cardiac muscle. *J. Biol. Chem.* **252**, 8731–8739.
- Prentki, M., and Madiraju, S.R.M. (2012). Glycerolipid/free fatty acid cycle and islet β -cell function in health, obesity and diabetes. *Mol. Cell. Endocrinol.* **353**, 88–100.
- Quirós, P.M., Ramsay, A.J., Sala, D., Fernández-Vizarrá, E., Rodríguez, F., Peinado, J.R., Fernández-García, M.S., Vega, J.A., Enríquez, J.A., Zorzano, A., et al. (2012). Loss of mitochondrial protease OMA1 alters processing of the GTPase OPA1 and causes obesity and defective thermogenesis in mice. *EMBO J.* **31**, 2117–2133.
- Rambold, A.S., Cohen, S., and Lippincott-Schwartz, J. (2015). Fatty acid trafficking in starved cells: regulation by lipid droplet lipolysis, autophagy, and mitochondrial fusion dynamics. *Dev. Cell* **32**, 678–692.
- Rogers, G.W., Brand, M.D., Petrosyan, S., Ashok, D., Elorza, A.A., Ferrick, D.A., and Murphy, A.N. (2011). High throughput microplate respiratory measurements using minimal quantities of isolated mitochondria. *PLoS One* **6**, e21746.
- Rosca, M.G., Vazquez, E.J., Kerner, J., Parland, W., Chandler, M.P., Stanley, W., Sabbah, H.N., and Hoppel, C.L. (2008). Cardiac mitochondria in heart failure: decrease in respirasomes and oxidative phosphorylation. *Cardiovasc. Res.* **80**, 30–39.
- Smirnova, E., Griparic, L., Shurland, D.L., and van der Bliek, A.M. (2001). Dynamin-related protein Drp1 is required for mitochondrial division in mammalian cells. *Mol. Biol. Cell* **12**, 2245–2256.
- Spinazzi, M., Casarin, A., Pertegato, V., Salviati, L., and Angelini, C. (2012). Assessment of mitochondrial respiratory chain enzymatic activities on tissues and cultured cells. *Nat. Protoc.* **7**, 1235–1246.
- Stone, S.J., Levin, M.C., Zhou, P., Han, J., Walther, T.C., and Farese, R.V., Jr. (2009). The endoplasmic reticulum enzyme DGAT2 is found in mitochondria-associated membranes and has a mitochondrial targeting signal that promotes its association with mitochondria. *J. Biol. Chem.* **284**, 5352–5361.
- Tarnopolsky, M.A., Rennie, C.D., Robertshaw, H.A., Fedak-Tarnopolsky, S.N., Devries, M.C., and Hamadeh, M.J. (2007). Influence of endurance exercise training and sex on intramyocellular lipid and mitochondrial ultrastructure, substrate use, and mitochondrial enzyme activity. *Am. J. Physiol. Regul. Integr. Comp. Physiol.* **292**, R1271–R1278.
- Twig, G., Elorza, A., Molina, A.J.A., Mohamed, H., Wikstrom, J.D., Walzer, G., Stiles, L., Haigh, S.E., Katz, S., Las, G., et al. (2008). Fission and selective fusion govern mitochondrial segregation and elimination by autophagy. *EMBO J.* **27**, 433–446.
- Twig, G., Liu, X., Liesa, M., Wikstrom, J.D., Molina, A.J.A., Las, G., Yaniv, G., Hajnóczky, G., and Shirihai, O.S. (2010). Biophysical properties of mitochondrial fusion events in pancreatic β -cells and cardiac cells unravel potential control mechanisms of its selectivity. *Am. J. Physiol. Cell Physiol.* **299**, C477–C487.
- Wang, H., Sreenivasan, U., Hu, H., Saladino, A., Polster, B.M., Lund, L.M., Gong, D.W., Stanley, W.C., Sztalryd, C., and Sztalryd, C. (2011). Perilipin 5, a lipid droplet-associated protein, provides physical and metabolic linkage to mitochondria. *J. Lipid Res.* **52**, 2159–2168.
- Wang, H., Sreenivasan, U., Gong, D.-W., O'Connell, K.A., Dabkowski, E.R., Hecker, P.A., Ionica, N., Konig, M., Mahurkar, A., Sun, Y., et al. (2013). Cardiomyocyte-specific perilipin 5 overexpression leads to myocardial steatosis and modest cardiac dysfunction. *J. Lipid Res.* **54**, 953–965.
- Wibom, R., Lundin, A., and Hultman, E. (1990). A sensitive method for measuring ATP-formation in rat muscle mitochondria. *Scand. J. Clin. Lab. Invest.* **50**, 143–152.

Wikstrom, J.D., Twig, G., and Shirihai, O.S. (2009). What can mitochondrial heterogeneity tell us about mitochondrial dynamics and autophagy? *Int. J. Biochem. Cell Biol.* *41*, 1914–1927.

Wikstrom, J.D., Mahdavian, K., Liesa, M., Sereda, S.B., Si, Y., Las, G., Twig, G., Petrovic, N., Zingaretti, C., Graham, A., et al. (2014). Hormone-induced mitochondrial fission is utilized by brown adipocytes as an amplification pathway for energy expenditure. *EMBO J.* *33*, 418–436.

Wittig, I., Braun, H.-P., and Schägger, H. (2006). Blue native PAGE. *Nat. Protoc.* *1*, 418–428.

Yu, J., Zhang, S., Cui, L., Wang, W., Na, H., Zhu, X., Li, L., Xu, G., Yang, F., Christian, M., and Liu, P. (2015). Lipid droplet remodeling and interaction with mitochondria in mouse brown adipose tissue during cold treatment. *Biochim. Biophys. Acta* *1853*, 918–928.

STAR★METHODS

KEY RESOURCES TABLE

REAGENT or RESOURCE	SOURCE	IDENTIFIER
Antibodies		
Mouse anti-Complex I NDUFB8	Thermo Fisher Scientific	Clone 20E9DH10C12, Cat. #459210; RRID: AB_2532232
Mouse anti-Complex II SDHB	Abcam	Clone EPR10880, Cat. #175225
Mouse anti-Complex III UQCRC1	Thermo Fisher Scientific	Clone 16D10AD9AH5, Cat. #459140; RRID: AB_2532227
Mouse anti-Complex 4 COX4	Thermo Fisher Scientific	Clone 1D6E1A8, Cat. #459600; RRID: AB_2532240
Mouse anti-ATP Synthase ATP5A1	Thermo Fisher Scientific	Clone 15H4C4, Cat. #43-9800; RRID: AB_2533548
Rabbit anti-TOM20	Santa Cruz Biotechnology	Cat. #11415; RRID: AB_2207533
Rabbit anti-UCP1	Abcam	Cat. #10983; RRID: AB_2241462
Mouse anti-DLP1 (Drp1)	BD Biosciences	Clone 8/DLP1, Cat. #611113; RRID: AB_398424
Mouse anti-OPA1	BD Biosciences	Clone 18/OPA1, Cat. #612607; RRID: AB_399889
Anti-mouse HRP-linked	Cell Signaling Technology	Cat. #7076S; RRID: AB_330924
Anti-rabbit HRP-linked	Cell Signaling Technology	Cat. #7074S; RRID: AB_2099233
Goat anti-Mouse IgG (H+L) Secondary Antibody, Alexa Fluor 488 conjugate	Thermo Fisher Scientific	Cat. #A11001; RRID: AB_2534069
Donkey anti-Rabbit IgG (H+L) Secondary Antibody, Alexa Fluor 546 conjugate	Thermo Fisher Scientific	Cat. #A10040; RRID: AB_2534016
Bacterial and Virus Strains		
Full-length Plin5 Adenovirus that includes mitochondrial recruiting sequence	Welgen	Ad-CMV- Plin5(aa1-463)-mKate2
Truncated Plin5 Δ 399–463 Adenovirus lacking mitochondrial recruiting sequence	Welgen	Ad-CMV- Plin5(aa1-399)-mKate2
mt-PAGFP Lentivirus	Twig et al., 2008	N/A
mt-DsRed Lentivirus	Twig et al., 2008	N/A
Biological Samples		
Interscapular brown adipose tissue from healthy 12-week-old male C57BL/6J	The Jackson Laboratory	Cat. #000664
Chemicals, Peptides, and Recombinant Proteins		
Fatty Acid-Free Bovine Serum Albumin	EMD Millipore	Cat. #126575
BODIPY 493/503 (4,4-Difluoro-1,3,5,7,8-Pentamethyl-4-Bora-3a,4a-Diaza-s-Indacene)	Thermo Fisher Scientific	Cat. #D3922
MitoTracker Deep Red FM	Thermo Fisher Scientific	Cat. #M22426
MitoTracker Green FM	Thermo Fisher Scientific	Cat. #M7514
Tetramethylrhodamine, Ethyl Ester, Perchlorate (TMRE)	Thermo Fisher Scientific	Cat. #T669
Ultrapure dimethyl sulfoxide (DMSO)	Amresco	Cat. #N182
Sodium Pyruvate	Thermo Fisher Scientific	Cat. #BP356
L-(–)-Malic Acid	Sigma-Aldrich	Cat. #M6413
Succinic Acid	Sigma-Aldrich	Cat. #S9512
Rotenone	Sigma-Aldrich	Cat. #R8875
Palmitoyl-L-carnitine chloride	Sigma-Aldrich	Cat. #P1645
Adenosine 5'-diphosphate monopotassium ADP	Sigma-Aldrich	Cat. #A5285
Oligomycin A	Sigma-Aldrich	Cat. #75351
FCCP	Sigma-Aldrich	Cat. #C2920
Antimycin A	Sigma-Aldrich	Cat. #A8674
NNN'N'-tetramethyl-p-phenylenediamine (TMPD)	Sigma-Aldrich	Cat. #T7394

(Continued on next page)

Continued

REAGENT or RESOURCE	SOURCE	IDENTIFIER
(+)-Sodium L-Ascorbate	Sigma-Aldrich	Cat. #A4034
Sodium Azide	Sigma-Aldrich	Cat. #S8032
Guanosine 5'-diphosphate sodium type I (GDP)	Sigma-Aldrich	Cat. #G7127
NuPAGE MES SDS Running Buffer (20×)	Thermo Fisher Scientific	Cat. #NP000202
NuPAGE Transfer Buffer (20×)	Thermo Fisher Scientific	Cat. #NP0006-1
NuPAGE LDS Sample Buffer	Thermo Fisher Scientific	Cat. #NP0007
Coomassie Brilliant Blue G-250	Amresco	Cat. #0615
Digitonin	Sigma-Aldrich	Cat. #D5628
Native PAGE 20× Running buffer	Thermo Fisher Scientific	Cat. #BN2001
NuPAGE 4%–12% Bis-Tris Protein Gels, 1.0 mm, 10-well	Thermo Fisher Scientific	Cat. #NP0321
NativePAGE 3%–12% Bis-Tris Protein Gels, 1.0 mm, 15-well	Thermo Fisher Scientific	Cat. #BN1003
Protease inhibitor cocktail	Santa Cruz	Cat. #24948A
5,5'-Dithiobis(2-nitrobenzoic acid) (DTNB)	Sigma-Aldrich	Cat. #D218200
Acetyl coenzyme A lithium salt	Sigma-Aldrich	Cat. #A2181
Oxaloacetic acid	Sigma-Aldrich	Cat. #O4126
Insulin from porcine pancreas	Sigma-Aldrich	Cat. #I5523
Rosiglitazone Maleate	Sigma-Aldrich	Cat. #1605817
BODIPY 558/568 C12 (4,4-Difluoro-5-(2-Thienyl)-4-Bora-3a,4a-Diaza-s-Indacene-3-Dodecanoic Acid)	Thermo Fisher Scientific	Cat. #D3835
Collagenase Type II	Worthington	Cat. #E11231
DMEM	Thermo Fisher Scientific	Cat. #31800022
RPMI 1640	Thermo Fisher Scientific	Cat. #12100046
Penicillin-Streptomycin	Thermo Fisher Scientific	Cat. #15140
Fetal calf serum	Thermo Fisher Scientific	Cat. #16000
Newborn calf serum	Sigma-Aldrich	Cat. #N4637
STEMPro Accutase	Thermo Fisher Scientific	Cat. #A1110501
Critical Commercial Assays		
Pierce BCA	Thermo Fisher Scientific	Cat. #23225
ECL Plus Western Blotting Substrate	Thermo Fisher Scientific	Cat. #32132
Free Glycerol Assay Kit	BioVision	Cat. #K630-100
ATP Bioluminescence Assay Kit CLS II	Roche	Cat. #11699695001
Experimental Models: Cell Lines		
Pre-adipocytes	Quirós et al., 2012	N/A
INS1 832/13	Twig et al., 2008	N/A
Software and Algorithms		
ImageJ	NIH	https://fiji.sc/
GraphPad	GraphPad Software	https://www.graphpad.com
Integrated Proteomics pipeline 2	Integrated Proteomics Applications	http://www.integratedproteomics.com/

CONTACT FOR REAGENT AND RESOURCE SHARING

Requests for information on methods and reagents should be directed to the Lead Contact Orian Shirihai (oshirihai@mednet.ucla.edu).

EXPERIMENTAL MODEL AND SUBJECT DETAILS

Mice

Mitochondria were isolated from 12-week-old male C57BL6/J mice and primary brown adipocytes were isolated from 3- to 4-week-old wild-type male C57BL6/J mice (Jackson lab, Bar Harbor, ME). Animals were fed standard chow (mouse diet 9F, PMI Nutrition International, Brentwood, MO) and maintained under controlled conditions (19–22°C and a 14:10 hr light-dark cycle) until euthanasia by isoflurane. All animal procedures were performed in accordance with the Guide for Care and Use of Laboratory Animals of the NIH, and were approved by the Animal Subjects Committee of the University of California, Los Angeles, and the Boston University Institutional Guidelines for Animal Care.

Cell Culture

Primary brown adipocytes isolation and culture: Brown adipose cells were isolated and cultured as described in (Cannon and Nedergaard, 2001b). BAT was dissected from interscapular, subscapular, and cervical regions of three male mice, minced, and transferred to 10 mL collagenase digestion buffer in 50 mL Falcon tube (2 mg/mL Collagenase Type II in 100 mM HEPES, 120 mM NaCl, 4.8 mM KCl, 1 mM CaCl₂, 4.5 mM Glucose, 1.5% BSA, pH 7.4). Collagenase digestion was performed in 37°C water incubator under constant agitation for 25 min with vortex agitation every 5 min. Digested tissue was homogenized with 18.5G needle and strained through 100 μm and 40 μm filters. 30 mL of ice-cold DMEM was added to tissue digest and centrifuged at 200 x g for 10 min at 4°C in Sorvall ST 16R (Thermo) with TX-200 swinging bucket rotor. Media was carefully removed and the cell pellet re-suspended in 30 mL ice-cold DMEM media. Cells were centrifuged again with the same settings. Next, the cell pellet was re-suspended in 5 mL growth medium (DMEM supplemented with 10% newborn calf serum (NCS), 4 mM Glutamine, 10 mM HEPES, 0.1 mg/mL sodium ascorbate, 50 U/mL penicillin, 50 μg/mL streptomycin) and plated in 6-well plate (Corning). Cells were incubated in 37°C 8% CO₂ incubator. 48 hr after isolation, the cells were washed to remove debris and media was replaced. 72 hr after isolation the cells were lifted using STEMPro Accutase, counted, and re-plated in differentiation media (growth media supplemented with 1 μM rosiglitazone maleate and 4 nM porcine insulin) in final experimental vessel. Cells were differentiated for 7 days and media was changed every other day. For transduction experiments, cells were transduced with virus in differentiation day 0–3.

Brown adipocyte immortalization: Brown preadipocytes immortalized by SV40T antigen were kindly provided by Drs. Pedro Quiros and Carlos Lopez-Otin (Quirós et al., 2012). Immortalized preadipocytes were differentiated for 7 days in culture medium supplemented with 20 nM insulin and 1 nM T3, 0.5 mM isobutylmethylxanthine, 0.5 μM dexamethasone, and 0.125 mM indomethacin (Fasshauer et al., 2000) in 37°C 5% CO₂ incubator.

INS1 culture: INS-1 832/13 cells were cultured in RPMI 1640 medium supplemented with 10% fetal calf serum (FBS), 10 mM HEPES buffer, 1 mM pyruvate, 50 μM 2-β-mercaptoethanol, 50 U/mL penicillin and 50 μg/mL streptomycin. Cells were incubated in 37°C 5% CO₂ incubator and used between passage 60 and 80.

METHOD DETAILS

Peridroplet Mitochondrial Isolation

All procedures were performed using pre-chilled equipment and solutions. Interscapular BAT from 6 mice was harvested and rinsed in PBS. Tissue was weighed, minced, and suspended in 6 mL (~1 mL/100 mg tissue) Sucrose-HEPES-EGTA buffer supplemented with BSA (SHE+BSA; 250 mM sucrose, 5 mM HEPES, 2 mM EGTA, 2% fatty acid-free BSA, pH 7.2). The preparation was then mechanically homogenized with 9 strokes in glass-teflon dounce homogenizer. The homogenate was then transferred to 50 mL falcon tube (Corning) and centrifuged in Sorvall ST 16R (Thermo) with TX-200 swinging bucket rotor at 900 x g for 10 min at 4°C. Supernatant was carefully poured into a new ice-cold falcon tube so as to leave the fat layer in the original tube. Keeping the original tube horizontal, the fat layer was scraped into a second ice-cold falcon tube and re-suspended in SHE+BSA buffer. The two fractions were centrifuged again at 900 x g for 10 min at 4°C and then transferred into 2 mL Eppendorf tubes and centrifuged in a microcentrifuge (Thermo) at 9,000 x g for 10 min at 4°C. The pellets were re-suspended in SHE+BSA and centrifuged with the same settings once more. The pellets were then re-suspended in SHE without BSA and protein concentration was determined by BCA (Thermo). BSA was omitted from the final isolation buffer to prevent interference with BCA assay.

Fluorescence Microscopy

Imaging Apparatus

All imaging was performed on Zeiss LSM710 and LSM880. Super-resolution imaging was performed with 63x Apochromat oil-immersion lens and AiryScan super-resolution detector (Huff et al., 2015). Low-resolution images were captured with 10x air objective. Live cell imaging was performed with humidified 5% CO₂ chamber on a temperature controlled stage.

Fluorophore Excitation/Emission

All fluorophores were excited on separate tracks to avoid artifacts due to bleed-through emission. DAPI was excited with 405 nm 30 mW laser and its emission captured through 485 nm short-pass filter. BODIPY 493/503, Alexa Fluor 488, MitoTracker green, and PAGFP were excited with 488 nm 25 mW Argon-ion laser and their emission captured through 500–550 nm band-pass filter. Alexa Fluor 546, TMRE, and mtDsRed were excited with 543 nm 1 mW Helium-Neon laser or 561 nm 20 mW diode-pumped

solid-state laser and their emission captured through a 580–650 nm band-pass filter. MitoTracker deep red was excited using 633 nm 5 mW Helium-Neon laser and its emission captured through a 645 nm long-pass filter.

Fat Layer and Isolated Mitochondria

1 μ L of re-suspended preparation was combined with 1 μ L SHE buffer supplemented with 1 μ M MitoTracker deep red and 1 μ M BODIPY 493/503 on a 1.0 mm glass slide (EMS 71867) and covered with #1.5 thickness coverglass (EMS 72222). Imaging was performed using 63x Apochromat oil-immersion lens.

Live Cells

Cells were seeded, transduced, and differentiated in glass-bottom confocal plates (MatTek P35G-0.170-14-C). On the day of the experiment, DAPI was loaded at 1 μ g/mL, BODIPY 493/503 was loaded at 200 nM and TMRE was loaded at 15 nM for 90 min followed by wash-out before imaging. DAPI and BODIPY were washed out while TMRE was present during imaging.

Image Analysis

All image analysis was performed in FIJI (ImageJ, NIH). Individual mitochondrial fluorescence intensity and area were measured in FIJI and imported into Microsoft Excel. Mitochondria smaller than 10 pixels in area were not included in final analyses. Mitochondria within 0.5 μ m of lipid droplet edge were defined as PDM while mitochondria beyond 0.5 μ m peridroplet region were defined as CM. Step-by-step instructions available upon request.

Image Presentation

Image contrast and brightness were not altered in any quantitative image analysis protocols. Brightness and contrast were optimized to properly display representative images in figure panels. Display settings are equivalent in images directly compared to one another (Figures 1B, 1C, 1F, 1I, 2J, 5B, 5G, and 7F).

Isolated Mitochondria Proteomics

100 μ g of isolated mitochondria were re-suspended in 6M Urea 100 mM Tris, pH 8.5 and then reduced and alkylated by incubation in 5 mM TCEP-HCL for 20 min at room temperature, in the dark (Langousis et al., 2016). Lys-C was introduced to the protein suspension at an enzyme to substrate ratio of 1:100, and incubated for 4 hr at 37°C. Samples were subsequently diluted to 2M Urea by addition of 100 mM Tris, pH 8.5. A final concentration of 1 mM CaCl₂ was added to the solution, and Trypsin introduced at an enzyme to substrate ratio of 1:50 overnight at 37°C. Proteolytic digestion was quenched by the addition of formic acid to a final concentration of 5%. Prior to mass spectrometric analysis, samples were desalted on Pierce C18 StageTips and eluted in 40% ACN before vacuum drying and resuspension in 5% formic acid. Desalted samples were separated on a 100 μ m internal diameter, reversed phase fused silica column packed with 18 cm of 1.9 μ m C18 particles (Dr. Maisch, GmbH) with an integrated 5 μ m pulled electrospray emitter. Gradient delivery as performed on an Easy nLC-1000 UHPLC at 300 nL/min, and MS/MS spectra generated by Data Dependent Acquisition on a Thermo Q-Exactive mass spectrometer. Data analysis was carried out using the Integrated Proteomics pipeline 2 (Integrated Proteomics Applications, San Diego, CA). Specifically, MS/MS spectra were searched with the ProLuCID algorithm, and PSM confidence was estimated by DTASelect. Search was performed against the Uniprot Mouse proteome containing only reviewed proteins, downloaded on 08/29/2016. Peptide spectrum identifications were filtered at a 1% maximum false detection rate as estimated by a target-decoy database search strategy. Protein identifications were only considered after reaching the requirement of a minimum of two confidently identified peptides. The IP2 pipeline provided normalized spectral abundance factor and spectral count calculations for set comparisons.

Isolated Mitochondria Respirometry

All procedures were performed with pre-chilled buffers, equipment, and consumables. Isolated mitochondria were re-suspended in respiration buffer (100 mM KCl, 10 mM KH₂PO₄, 2 mM MgCl₂, 5 mM HEPES, 1 mM EGTA, 0.1% BSA, 1 mM GDP, pH 7.2) and kept on ice as described previously (Mahdavian et al., 2017). Four micrograms per well were loaded into Seahorse XF96 microplate in 20 μ L volume containing substrates. The loaded plate was centrifuged at 2,000 \times g for 5 min at 4°C and an additional 115 μ L of buffer+substrate was added to each well. Substrate concentrations were as follow: 5 mM Pyruvate + 5 mM Malate, 5 mM Succinate + 2 μ M Rotenone, 40 μ M palmitoyl-Carnitine + 1 mM Malate. ADP was injected at port A (3.5 mM final concentration), oligomycin at port B (3.5 μ M), FCCP at port C (4 μ M) and Antimycin A at port D (4 μ M). Mix and measure times were 0.5 min and 4 min, respectively. A 2 min wait time was included for oligomycin-resistant respiration measurements.

Cytochrome c Oxidase Assay

Isolated mitochondria were re-suspended in ice-cold respiration buffer and kept on ice. Two micrograms of isolated mitochondria were re-suspended in respiration buffer and plated on a seahorse XF96 microplate 20 μ L volume. Cytochrome c oxidase activity was exclusively assessed using 100 μ M N,N,N',N'-Tetramethyl-p-phenylenediamine (TMPD) and 10 mM ascorbate as previously described in detail (Divakaruni et al., 2014). To exclude respiration mediated by TCA and other electron transport complexes, we injected antimycin/rotenone injection at the start of the assay. We injected the COX-specific inhibitor sodium azide at the end of the assay to confirm that TMPD/ascorbate-driven respiration was specific to COX activity.

ATP Synthesis Assay

20 μ g of isolated mitochondria were re-suspended in 1 mL of mitochondrial respiration buffer containing 5 mM pyruvate + 5 mM malate + 3.5 mM ADP and kept on ice (Wibom et al., 1990). 50 μ L of this mixture was combined with 50 μ L of Luciferin-luciferase

mix in clear-bottom black 96-well plate (Corning) and measured immediately. We determined the optimal concentration of reagents and measurement settings on our instrument using HPLC-purified ATP standards. Luminescent counts were integrated over 0.5 s at 10 s intervals separated by 0.5 s orbital shaking on Spark M10 microplate reader (Tecan). To control for non-OXPHOS ATP, we assessed luminescence in parallel samples that were treated with the ATP synthase inhibitor oligomycin A. We confirmed minimal ATP contamination in the ADP preparation was minimal by assaying ADP independently. The linear rate of luminescence increase was calculated to determine ATP synthesis rate.

Protein Gel Electrophoresis and Immunoblotting

SDS-PAGE

10–20 μg of isolated mitochondrial protein was re-suspended in NuPAGE LDS Sample Buffer with protease inhibitor cocktail and incubated at 45°C for 10 min. Samples were then loaded into 4%–12% Bis-Tris precast gels (ThermoFisher Sci. NP0321) and electrophoresed in xCell SureLock (Novex) in constant voltage at 60V for 15 min (to clear stacking) and 150V for 45 min.

Blue Native Gel Electrophoresis

10–50 μg of isolated mitochondrial protein was re-suspended in 20 μL solubilization buffer (50 mM Imidazole, 500 mM 6-aminohexanoic acid, EDTA 1 mM pH 7.0) (Wittig et al., 2006). 8 mg digitonin/mg of mitochondrial protein was added and samples were incubated on ice for 5 min. Since commercial digitonin is only 50% pure, we used 16 mg of crude powder to achieve 8 mg (no re-crystallization). Digitonin was dissolved in PBS by boiling and stored at 4°C until use. Solubilized samples were centrifuged at maximal speed in a microcentrifuge (Thermo) for 30 min at 4°C. Pellet was discarded and supernatant was combined with 1 μL of 2.5% Coomassie G-250. Samples were loaded into NativePAGE 3%–12% Bis-Tris gel and electrophoresed at 4°C in xCell SureLock (Novex) in constant voltage at 20V for 60 min and 200V for 120 min or until dye front exited the gel.

Immunoblotting

Proteins were transferred to methanol-activated PVDF membrane in xCell SureLock in 30V constant voltage for 1 hr at 4°C. Coomassie was completely washed off blue native blots using 100% methanol. Blots were blocked with 5 g/100 mL non-fat dry milk in 0.5 mL/L PBST (1 mL/L Tween-20/PBS) and incubated with primary antibody diluted in 1 g/100 mL BSA/PBST overnight at 4°C. The next day, blots were washed 3x10 min in PBST, probed with HRP-linked secondary antibodies diluted in blocking solution for 1 hr at room temperature, and rinsed again 3x10 min in PBST. Detection was achieved by ECL-Plus reagent and imaging was performed with Typhoon 9410 Molecular Imager (Amersham). Image contrast was uniformly reduced to enhance visibility. Band densitometry was quantified using ImageJ Gel Plugin (NIH).

Immunofluorescence

Cells were cultured, transduced, and differentiated on coverslips and fixed at 4% vol/vol PFA for 15 min at room temperature. After washing in PBS, cells were incubated in permeabilization buffer (2 $\mu\text{L}/\text{mL}$ Triton X-100, 0.5 mg/mL Sodium Deoxycholate in PBS, pH 7.4) for 15 min at room temperature. Cells were then blocked with 3 g/100 mL BSA for 1 hr at room temperature. Next, cells were incubated with 1:200 primary antibody at 4°C overnight. The next day, cells were washed in PBS and incubated with 1:500 Anti-Mouse Alexa Fluor 488 or Anti-Mouse Alexa Fluor 546 secondary antibodies for 1 hr at room temperature. After washing in PBS, coverslips were mounted in MOWIOL on glass slide, air-dried, and stored at 4°C.

Citrate Synthase Assay

Citrate synthase activity was performed using 5,5'-Dithiobis(2-nitrobenzoic acid) (DTNB) (Spinazzi et al., 2012). Isolated mitochondria were re-suspended in 200 mM Tris buffer containing 0.2% v/v Triton X-100 (pH 8.0), 100 μM DTNB, and 300 μM acetyl-CoA and loaded into a clear-bottom black 96-well plate. Baseline 412 nm absorbance was measured using Spark M10 microplate reader (Tecan). Oxaloacetate was then added and 412 nm absorbance was repeatedly measured at 20 s intervals. The linear rate of absorbance increase was calculated to determine citrate synthesis rate.

NADH Imaging

NADH autofluorescence was excited using 730 nm 2-photon Chameleon Vision laser (Coherent) to give 365 nm photo-equivalence at the focal plane. 425–475 nm emission was detected by ultra-high sensitivity Gallium Arsenide Phosphide detectors with non-descanned beampath to maximize emission collection and minimize laser power. To minimize artifacts due to phototoxicity and bleaching, image acquisition settings were optimized on a test cell that was not included in final image analysis. Images of analyzed cells were subsequently acquired using a single laser scan.

Electron Microscopy

Interscapular brown adipose tissue was harvested from mice acclimated to 28°C for 2–4 weeks and from mice acclimated to 6°C for 1–5 days. Small tissue fragments were fixed in 2% glutaraldehyde/2% paraformaldehyde in 0.1M phosphate buffer, pH 7.4, for 4 hr at room temperature (Cinti et al., 2002). Samples were post-fixed in 1% osmium tetroxide, dehydrated in ethanol, and embedded in epoxy resin. Thin sections were obtained by MTX ultramicrotome (RMC, Tucson, AZ), stained with lead citrate, and imaged with Philips CM10 transmission electron microscope (Philips, Eindhoven, Netherlands). Imaging of cross-ruled grating of known distance was used to calibrate images.

Image analysis: Mitochondria were manually traced in electron micrographs and quantified in ImageJ. Aspect ratio was calculated as the major axis divided by the minor axis.

Virus Preparation

Plin5 and Plin5 Δ 399-463 constructs were a generous gift from Carole Sztalyrd (Wang et al., 2011). Plasmids were modified to express mKATE2 far-red fluorophore to enhance compatibility with fluorescent dyes and packaged into adenoviral particles (Welgen). Viral transduction was confirmed by mKATE2 fluorescence. Lentiviral particles for mtPAGFP, mtDsRed, and DRP1DN were generated as previously described in detail (Wikstrom et al., 2014).

Gene Delivery

Pre-adipocytes and INS1 cells were incubated with 0.3 μ L/mL of adenoviral preparation for 5 hr in complete culture media. This was sufficient to achieve transduction in the majority of cells with little to no toxicity as assessed by cell division and viability. Fluorescent label and protein expression were detectable at differentiation day 7. Lentiviruses were delivered as previously described in detail (Wikstrom et al., 2014).

Lipolysis Assay

Cells were seeded, transduced, and differentiated in 96-well plate. On the day of experiment, the cells were washed once and incubated with 100 μ L Krebs-Ringer Bicarbonate Buffer (KRB; 119 mM NaCl, 4.6 mM KCl, 5 mM NaHCO₃, 2 mM CaCl₂, 1 mM MgSO₄, 0.15 mM Na₂HPO₄, 0.4 mM KH₂PO₄, 20 mM HEPES, 5 mM Glucose, pH 7.4) for 2 hr. KRB was collected and assayed for glycerol using Free Glycerol Colorimetric/Fluorometric Assay Kit (BioVision) according to the manufacturer instructions.

Thin-Layer Chromatography

Cells were seeded, transduced, and differentiated in 6-well plate. Cells were washed and incubated with overnight with 1 μ M BODIPY C12 558/568 as previously described (Rambold et al., 2015). Cells were harvested using Accutase and spun down. Cellular lipids were extracted in chloroform and developed on aluminum-backed silica plates (Sigma 55811) using 1:2 cyclohexane:ethyl acetate. Plates were imaged using Typhoon 9410 Molecular Imager (Amersham) and spots were quantified using ImageJ Gel Plugin.

Mitochondrial Fusion Assay

Brown adipocytes were seeded, transduced, and differentiated in glass-bottom confocal plates (MatTek). mtPAGFP was activated using 750 nm 2-photon Chameleon Vision laser (Coherent) to give 375 nm photo-equivalence at the focal plane (Twig et al., 2008, 2010). The diffusion of mtPAGFP was assessed by repeatedly scanning the cell at 15 min intervals. GFP fluorescence was quantified within the region of interest at every time point to assess diffusion. Diffusion of cytoplasmic mitochondria PAGFP reached as steady state within 40-50 min after photo-activation. At this time point, mitochondria that retained non-diluted GFP were defined as non-fusing mitochondria.

QUANTIFICATION AND STATISTICAL ANALYSIS

All data analyses were performed using GraphPad Prism 5 and Microsoft Excel. Raw data from each individual experiment was evaluated using an unpaired two-tailed t test with 95% confidence in Prism. For datasets that did not pass the D'Agostino and Pearson omnibus normality test ($\alpha = 0.05$), differences were evaluated using a two-tailed unpaired non-parametric Mann-Whitney test with 95% confidence. For repeated independent experiments, the raw data of CM and PDM from each individual experiment were normalized to the average value of all mitochondria in that specific experiment as shown in the formula below. Experiment-normalized data were then evaluated by a paired two-tailed t test with 95% confidence.

$$CM_{\text{normalized}} = \frac{\sum CM_{\text{raw values}} / \text{number of CM replicates}}{(\sum CM_{\text{raw values}} + \sum PDM_{\text{raw values}}) / \text{total number of CM and PDM replicates}}$$

$$PDM_{\text{normalized}} = \frac{\sum PDM_{\text{raw values}} / \text{number of PDM replicates}}{(\sum CM_{\text{raw values}} + \sum PDM_{\text{raw values}}) / \text{total number of CM and PDM replicates}}$$